Monthly Notices
of the
ROYAL ASTRONOMICAL SOCIETY

MNRAS **481,** 4009–4029 (2018)
Advance Access publication 2018 September 7

doi:10.1093/mnras/sty2463

On the formation history of Galactic double neutron stars

Alejandro Vigna-Gómez,[1,2]★ Coenraad J. Neijssel,[1] Simon Stevenson,[1,3] Jim W. Barrett,[1] Krzysztof Belczynski,[4] Stephen Justham,[5,6,7,2] Selma E. de Mink,[7] Bernhard Müller,[8] Philipp Podsiadlowski,[9,2] Mathieu Renzo,[7] Dorottya Szécsi[1] and Ilya Mandel[1,2,8]

[1]*Birmingham Institute for Gravitational Wave Astronomy and School of Physics and Astronomy, University of Birmingham, Birmingham, B15 2TT, UK*
[2]*DARK, Niels Bohr Institute, University of Copenhagen, Blegdamsvej 17, DK-2100 Copenhagen, Denmark*
[3]*OzGrav, Swinburne University of Technology, Hawthorn VIC 3122, Australia*
[4]*Nicolaus Copernicus Astronomical Center, Polish Academy of Sciences, ul. Bartycka 18, PL-00-716 Warsaw, Poland*
[5]*School of Astronomy, Space Science, University of the Chinese Academy of Sciences, Beijing 100012, China*
[6]*National Astronomical Observatories, Chinese Academy of Sciences, Beijing 100012, China*
[7]*Anton Pannekoek Institute for Astronomy, University of Amsterdam, NL-1090 GE Amsterdam, the Netherlands*
[8]*Monash Centre for Astrophysics, School of Physics and Astronomy, Monash University, Clayton, Victoria 3800, Australia*
[9]*Department of Astronomy, Oxford University, Oxford OX1 3RH, UK*

Accepted 2018 September 6. Received 2018 September 5; in original form 2018 May 21

ABSTRACT

Double neutron stars (DNSs) have been observed as Galactic radio pulsars, and the recent discovery of gravitational waves from the DNS merger GW170817 adds to the known DNS population. We perform rapid population synthesis of massive binary stars and discuss model predictions, including DNS formation rates, mass distributions, and delay time distributions. We vary assumptions and parameters of physical processes such as mass transfer stability criteria, supernova natal kick distributions, remnant mass prescriptions, and common-envelope energetics. We compute the likelihood of observing the orbital period–eccentricity distribution of the Galactic DNS population under each of our population synthesis models, allowing us to quantitatively compare the models. We find that mass transfer from a stripped post-helium-burning secondary (case BB) on to a neutron star is most likely dynamically stable. We also find that a natal kick distribution composed of both low (Maxwellian $\sigma = 30\,\mathrm{km\,s^{-1}}$) and high ($\sigma = 265\,\mathrm{km\,s^{-1}}$) components is preferred over a single high-kick component. We conclude that the observed DNS mass distribution can place strong constraints on model assumptions.

Key words: binaries: general – stars: neutron – pulsars: general.

1 INTRODUCTION

Since the first detection of a Galactic double neutron star (DNS) system (Hulse & Taylor 1975), the growing observed population of DNSs continues to provide constraints on their orbital parameters. Precise measurements of Keplerian and post-Keplerian parameters (Kramer et al. 2006) contain valuable information about the progenitors and formation history of neutron star (NSs) and DNSs. Additionally, GW170817 (Abbott et al. 2017c) became the first gravitational-wave signal detected from a DNS merger. These precise measurements allow us to test our understanding on the massive binary progenitor populations and their formation history (e.g. Bhattacharya & van den Heuvel 1991).

Tutukov & Yungel'son (1993) carried out an early rapid population synthesis study of Galactic NSs. The formation and fate of DNSs has been studied with a similar approach by Portegies Zwart & Yungelson (1998) who made an analysis of the observed systems and predictions of gamma-ray burst (GRB) rates, and Belczyński & Bulik (1999) who focused on gravitational-wave merger rates. Voss & Tauris (2003) studied both GRB and gravitational-wave merger rates for Galactic DNSs and binary black holes (BHs). O'Shaughnessy et al. (2005) used six DNSs observed in the Galactic disc to constrain population synthesis models. Several binary population synthesis studies have focussed on natal kick distributions (e.g. Brandt & Podsiadlowski 1995; Podsiadlowski et al. 2004; Bray & Eldridge 2016), short GRBs locations (e.g. Church et al. 2011), evolutionary channels (e.g. Andrews et al. 2015), and merger rates (e.g. Chruslinska et al. 2018). More recently, Kruckow et al. (2018) used their population synthesis model,

★ E-mail: avigna@star.sr.bham.ac.uk

Table 1. Measured parameters of the Galactic DNSs used as a diagnosis in this study.

Pulsar	P (d)	e	$M_{\rm plsr}$ ($M_\odot$)	$M_{\rm cmpn}$ ($M_\odot$)	Ref.
J0453+1559	4.072	0.113	1.559	1.174	*a*
J0737–3039†, ‡	0.102	0.088	1.338	1.249	*b*
B1534+12†	0.421	0.274	1.333	1.346	*c*
J1756–2251†	0.320	0.181	1.341	1.230	*d*
B1913+16†	0.323	0.617	1.440	1.389	*e*
J1913+1102†	0.206	0.090	1.580	1.300	*f*
J1757–1854†	0.184	0.606	1.338	1.395	*g*
J1518+4904⋆	8.634	0.249	–	–	*h*
J1811–1736⋆	18.779	0.828	–	–	*i*
J1829+2456⋆	1.176	0.139	–	–	*j*
J1930–1852⋆	45.060	0.399	–	–	*k*
J1753–2240⋆	13.638	0.304	–	–	*l*
J1411+2551⋆	2.616	0.169	–	–	*m*
J1946+2052⋆	0.078	0.064	–	–	*n*

Notes. †Systems which will merge in via gravitational-wave emission in less than 3000 Myr. ‡Double pulsar. ⋆Measurements used only for diagnosis in the P–e plane. The masses of the DNSs are presented as $M_{\rm plsr}$ and $M_{\rm cmpn}$, the mass of the pulsar and the companion, respectively.
References: [a]Martinez et al. (2015); [b]Kramer et al. (2006); [c]Fonseca, Stairs & Thorsett (2014); [d]Faulkner et al. (2005); [e]Hulse & Taylor (1975); [f]Lazarus et al. (2016); [g]Cameron et al. (2018); [h]Janssen et al. (2008); [i]Corongiu et al. (2007); [j]Champion et al. (2004); [k]Swiggum et al. (2015); [l]Keith et al. (2009); [m]Martinez et al. (2017); [n]Stovall et al. (2018).

calibrated to match the observed Galactic DNS population, to predict merger rates in the local Universe.

Using the rapid population synthesis element of the Compact Object Mergers: Population Astrophysics and Statistics (COMPAS) suite (Stevenson et al. 2017), we use the Galactic DNS population as an observational constraint on massive binary evolution, from two zero age main-sequence stars (ZAMS) to a pair of NSs. The COMPAS tool simulates isolated binaries: double star systems that evolve without significant interaction with the environment or with other stars. The majority of the confirmed Galactic DNSs [14 confirmed systems (for details, see Table 1) as well as Tauris et al. (2017) and references therein] come from isolated binaries that lie in the Galactic disc. We do not address the two Galactic globular cluster binaries in this work, B2127+11C (Anderson et al. 1990) and J1807–2500B (Lynch et al. 2012, not a confirmed DNS), since dynamical interactions likely played a key role in their formation (Phinney & Sigurdsson 1991; Grindlay, Portegies Zwart & McMillan 2006; Ivanova et al. 2008).

Our paper explores the impact of physical interactions during various stages of binary evolution on predictions of observables such as orbital parameters of Galactic DNSs and inferred mass distributions of gravitational-wave events. To do this, we compare models with different underlying assumptions and quantify the difference between their predictions. For each model, we provide DNS formation rates and orbital parameters as predictions to be tested against present time observations. We compare the predicted DNS masses ($m_{1,2}$) and orbital parameters (period P, eccentricity e) to those of the observed Galactic DNSs. We find that the natal kicks received by NSs during formation in a supernova (SN) and mass transfer stability criteria play a fundamental role in recreating the Galactic DNS population.

The paper is structured as follows. Section 2 describes population synthesis and presents our `Fiducial` model. Changes made to binary evolution in COMPAS since Stevenson et al. (2017) are specified. Section 3 presents the results of the `Fiducial` population, with particular emphasis on the formation history of Galactic DNSs. The effect of variations such as mass transfer during the post-helium-burning phase and the comparison between different natal kick distributions is mentioned. We conclude with a summary and discussion in Section 4.

2 METHODS

2.1 Population synthesis

The COMPAS suite includes a rapid population synthesis module designed to simulate isolated binary evolution. Rapid population synthesis aims to simulate the evolution of a binary system in a fraction of a second, which makes it possible to simulate millions of binaries in a few days using a single processor. The population synthesis module of COMPAS explores binary evolution with a Monte Carlo simulation. We stochastically sample the initial distribution of binary masses, separations, and eccentricities in order to generate a population.

Given a certain mass and certain metallicity value at ZAMS, we define the initial conditions and evolution of a star following the fitting formulae of single-star evolution (SSE) as given in Hurley, Pols & Tout (2000) to the detailed models calculated in Pols et al. (1998). We use the same nomenclature as Hurley et al. (2000) to define stellar phases, such as the Hertzsprung gap (HG), where the HG is defined as the phase after the depletion of hydrogen during the main sequence (MS) and before the start of core helium burning (CHeB). For every binary, we follow the centre of mass evolution of the system, computing the masses, separation and eccentricity at every time-step. We use parametrizations to quantify the effect on the orbit of the physics involving mass-loss through stellar winds, mass transfer, SNe, and common-envelope (CE) events. For SNe, we also use remnant mass distributions that will determine the ultimate fate of our stars. Each binary is evolved until the system either merges, becomes unbound, or forms a double compact object (DCO). The population generates a set of DCOs, where DNSs are sub-selected into our final distribution of interest. COMPAS population synthesis is similar to the general approach of the codes SeBa (Portegies Zwart & Verbunt 1996; Portegies Zwart & Yungelson 1998; Toonen, Nelemans & Portegies Zwart 2012), BSE (Hurley, Tout & Pols 2002), StarTrack (Belczynski, Kalogera & Bulik 2002; Belczynski et al. 2008), and binary_c (Izzard et al. 2004, 2006, 2009), all of which use the SSE fits from Hurley et al. (2000).

Our current approach to the study of populations by proposing an initial model and studying the variations is similar to the one described in Dominik et al. (2012). That study uses StarTrack to simulate populations from ZAMS to DCO formation and predict merger rates for all compact objects. Their 'Standard' model overlaps with some of our `Fiducial` model assumptions.

2.2 `Fiducial` model

2.2.1 Changes since Stevenson et al. (2017)

The main changes to binary evolution modelling in COMPAS relative to the default assumptions in Stevenson et al. (2017), hereafter referred to as COMPAS_α, are as follows:

(i) Incorporation of the fitting formulae of the binding energy parameter $\lambda_{\rm Nanjing}$ instead of a fixed $\lambda = 0.1$, as described in Section 2.2.5.

(ii) A bimodal natal kick distribution, where core-collapse supernova (CCSN) explosions contribute to the high mode ($\sigma_{\rm high} = 265\,{\rm km\,s^{-1}}$), while ultra-stripped supernova (USSN) explosions and electron-capture supernova (ECSN) explosions constitute the low mode ($\sigma_{\rm low} = 30\,{\rm km\,s^{-1}}$), as described in Section 2.2.3.

(iii) Mass transfer stability criteria, allowing for always stable case BB mass transfer, as described in Section 2.2.5.

(iv) The 'optimistic' CE assumption, which allows donors classified as HG stars in the Hurley et al. (2000) models to engage and survive a CE phase, as described in Section 2.2.5.

2.2.2 *Initial distributions*

To initialize a binary, we sample from initial distributions of mass, separation, and eccentricity of the binary at ZAMS. For the mass distribution, we draw the primary mass from a Kroupa initial mass function (IMF; Kroupa 2001) in the form $dN/dm_1 \propto m_1^{-2.3}$ with masses between $5 \leq m_1/{\rm M}_\odot \leq 100$. The secondary is drawn from a flat distribution in mass ratio between $0.1 < q_{\rm ZAMS} \equiv m_2/m_1 \leq 1$ (Sana et al. 2012). The initial separation follows the flat-in-the-log distribution (Öpik 1924; Sana et al. 2012) in the range $0.1 < a_{\rm ZAMS}/{\rm au} < 1000$. We assume that all of our binaries are circular at ZAMS, with $e_{\rm ZAMS} = 0$.

2.2.3 *Supernovae*

We differentiate between three SN scenarios: CCSN, ECSN, and USSN. For the CCSN treatment, we apply the 'rapid' explosion mechanism,[1] as presented in Fryer et al. (2012), to determine the compact object remnant mass according to the total and carbon–oxygen (CO) core mass of the progenitor, with a maximum allowed NS mass of $m_{\rm NS,max} = 2.0\,{\rm M}_\odot$. In this explosion mechanism, the collapse does not allow for accretion on to the proto-NS, and is able to reproduce the apparent mass gap between NSs and BHs (Özel et al. 2010; Farr et al. 2011). There is no consensus yet whether the mass gap is due to observational selection effects or if it is intrinsic to the explosion mechanism (Kreidberg et al. 2012; Wyrzykowski et al. 2016).

Another explosion scenario that some of our binary systems experience is called USSNe (Tauris et al. 2013; Tauris, Langer & Podsiadlowski 2015). In this case, a star becomes stripped when it loses its hydrogen envelope during its evolution; if, during later stages, it manages to lose its helium envelope, it becomes ultra-stripped. In COMPAS, any star that engages in a stable case BB mass transfer episode with an NS as an accretor is considered to be ultra-stripped. We define case BB as a mass transfer episode that involves a post-helium main-sequence (HeMS) donor star that has stopped burning helium in the core (helium Hertzsprung gap, HeHG). Ultra-stripped stars are left with an ONeMg core with a thin carbon and helium layer (Tauris et al. 2013). The compact object remnant mass of an USSN is determined in the same way as for CCSN.

A single star with mass within $7 \lesssim m_{\rm ZAMS}/{\rm M}_\odot \lesssim 10$ may collapse in an ECSN. Early studies by Nomoto (1984, 1987) had a higher mass range for single stars between $8 \lesssim m_{\rm ZAMS}/{\rm M}_\odot \lesssim 10$, while more recent studies propose a lower mass range from $7 \lesssim m_{\rm ZAMS}/{\rm M}_\odot \lesssim 9$ (Woosley & Heger 2015). Note that binary interactions extend this initial mass range, which means that if we take a COMPAS simulation with binaries, the mass range for ECSNe will be broader because binarity changes the progenitor ZAMS masses (i.e. initially less massive stars that accreted mass or initially more massive that lost mass). We assume the baryonic mass of the degenerate ONeMg core leading to an ECSN is $1.38\,{\rm M}_\odot$ (Nomoto 1987). We approximate the ECSN remnant mass as $m_{\rm ECSN} = 1.26\,{\rm M}_\odot$ using the quadratic approximation $m_{\rm bar} - m_{\rm grav} = 0.075 m_{\rm grav}^2$ (Timmes, Woosley & Weaver 1996).

All natal kicks from SNe are assumed to be isotropic in the frame of reference of the exploding star and randomly drawn from a unit sphere. For the magnitude of the natal kicks of the SNe, we assume a bimodal distribution (e.g. Katz 1975; Arzoumanian, Chernoff & Cordes 2002). For CCSN, we draw natal kick magnitudes from a Maxwellian velocity distribution with a one-dimensional (1D) standard deviation of $\sigma_{\rm high} = 265\,{\rm km\,s^{-1}}$ following the three-dimensional (3D) pulsar velocity distribution derived by Hobbs et al. (2005) from a subset of their two-dimensional (2D) observations. USSN and ECSN natal kick magnitudes are drawn from a Maxwellian velocity distribution with a 1D standard deviation of $\sigma_{\rm low} = 30\,{\rm km\,s^{-1}}$, following Pfahl, Rappaport & Podsiadlowski (2002a) and Podsiadlowski et al. (2004). This second component is introduced to match the observed low natal kicks in some Galactic DNSs (Schwab, Podsiadlowski & Rappaport 2010; Beniamini & Piran 2016) as well as in isolated pulsars (Brisken et al. 2002), as the single-mode isolated pulsar velocity distribution proposed by Hobbs et al. (2005) fails to predict the low-velocity pulsar population as discussed by Verbunt, Igoshev & Cator (2017) and Verbunt & Cator (2017).

2.2.4 *Mass transfer*

A crucial part of binary evolution is mass transfer, which begins when one or both stars fill their Roche lobe (Eggleton 1983), instigating a Roche-lobe overflow (RLOF) event. In our population synthesis approach, mass transfer is treated by determining stability, time-scales, and conservativeness. Rapid population synthesis oversimplifies the complex hydrodynamics involved in a mass transfer episode. There have been some efforts to provide generalized models (e.g. de Mink, Pols & Hilditch 2007; Claeys et al. 2014; Tauris et al. 2015). In particular, determining whether mass transfer is dynamically stable is challenging (e.g. Pavlovskii et al. 2017).

To determine dynamical stability during mass transfer episodes, we compare the response of the donor star's radius to adiabatic mass-loss, $\zeta_{\rm ad} = ({\rm d}\log R/{\rm d}\log M)_{\rm ad}$, to the response of the Roche-lobe radius of the donor, $\zeta_{\rm RL}$, under the same mass exchange conditions. Mass transfer is defined as dynamically stable if $\zeta_{\rm ad} \geq \zeta_{\rm RL}$. We use fixed values of $\zeta_{\rm ad,\,MS} = 2.0$ for MS and $\zeta_{\rm ad,\,HG} = 6.5$ for HG stars that are typical for these phases, following models by Ge et al. (2015). For later phases in which the stars still possess hydrogen envelopes (such as the phases CHeB and early asymptotic giant branch, EAGB), we use a fit to $\zeta_{\rm ad} = \zeta_{\rm SPH}$ for condensed polytrope models of a red giant as provided in Soberman, Phinney & van den Heuvel (1997). Case BB mass transfer is always stable in the `Fiducial` model, broadly in agreement with Tauris et al. (2015).

COMPAS uses fits to equilibrium mass–radius relations (Hurley et al. 2000) to describe stellar evolution. We use these analytic formulae to determine when stable mass transfer is driven

[1] In this text, the term SN explosion *scenario* refers to the type of explosion, such as ECSN, USSN, or CCSN, while the term explosion *mechanism* refers to the numerical treatment of this process in the code. The latter is henceforth also referred to as SN prescription, or fallback prescription, or remnant mass model.

by thermal readjustment. If the calculated donor-star radius cannot stay within its Roche lobe during thermally stable mass transfer, then we remove the mass on a thermal time-scale, although our stellar evolution recipes do not accurately represent the donor stars during thermal-time-scale mass transfer (for more detailed studies, see e.g. Kippenhahn & Weigert 1967; Pols 1994). Once the donor's calculated equilibrium radius can again fit within its Roche lobe, we assume that the mass transfer occurs on a nuclear time-scale (Claeys et al. 2014).

Dynamically stable mass transfer from evolved stars is assumed to always proceed on the thermal time-scale until the entire envelope is removed (but see e.g. Götberg, de Mink & Groh 2017). We approximate the thermal time-scale as the Kelvin–Helmholtz time-scale of the donor's envelope, $\tau_{\rm KH} = GMM_{\rm env}/RL$, where G is the gravitational constant, M is the total mass, $M_{\rm env}$ is the mass of the envelope, R is the radius, and L is the luminosity of the star.

Conservativeness is defined as the amount of transferred mass from the donor that the accretor will accept and retain. When mass is lost from the system during non-conservative mass transfer, the fraction of mass lost and the specific angular momentum it carries away determine the orbital parameters and subsequent evolution of the system. In the `Fiducial` model, if mass transfer is non-conservative, the non-accreted mass is lost from the vicinity of the accreting star via isotropic re-emission, carrying away the specific orbital angular momentum of the accretor. The conservativeness of our mass transfer episode is limited by the accretor. For non-degenerate accretors, we assume a star can accrete at a maximum rate $\dot{M}_{\rm acc} = C M_{\rm acc}/\tau_{\rm KH}$. We use $C = 10$ following Hurley et al. (2002). For degenerate accretors, we assume the compact object accretion is limited by the Eddington accretion limit.

2.2.5 *Common envelope*

If either of the binary stars begin dynamically unstable mass transfer, the binary may become engulfed in a CE phase. The loss of corotation between the binary system and the envelope generates drag forces, which causes the binary to inspiral. The gravitational energy lost from the orbit is deposited in the envelope and may be enough to eject it from the binary. The whole process allows the system to decrease its separation several orders of magnitude.

The classical isolated binary evolutionary scenario for the formation of DCOs often involves a CE phase (Paczynski 1976; Ivanova et al. 2013; Belczynski et al. 2016). We use the $\alpha\lambda$ formalism, as proposed by Webbink (1984) and de Kool (1990), to estimate the effect of the CE phase on the orbit of the binary.

The value of λ, which parametrizes the envelope's binding energy, is calculated from detailed models of the stellar structure. For our `Fiducial` model, we adopt $\lambda_{\rm Nanjing}$ (originally referred to as $\lambda_{\rm b}$, which includes internal energy) as calculated by Xu & Li (2010). This $\lambda_{\rm Nanjing}$ is also implemented in the StarTrack code (Dominik et al. 2012).

The value of α, which parametrizes the efficiency of converting orbital energy into unbinding the envelope, depends on the orbital parameters, energy sources, and energy exchange during the CE phase, and is difficult to constrain even with detailed hydrodynamical models (Ivanova et al. 2013). We use $\alpha = 1$. We assume that the orbit is always circularized during a CE phase. We allow donor stars that engage into a CE phase during the HG to survive the event and expel the CE if allowed by the energy condition. This assumption is labelled 'optimistic' CE in the literature (Dominik et al. 2012), while the alternative, 'pessimistic' CE, always leads to a merger for HG donors.

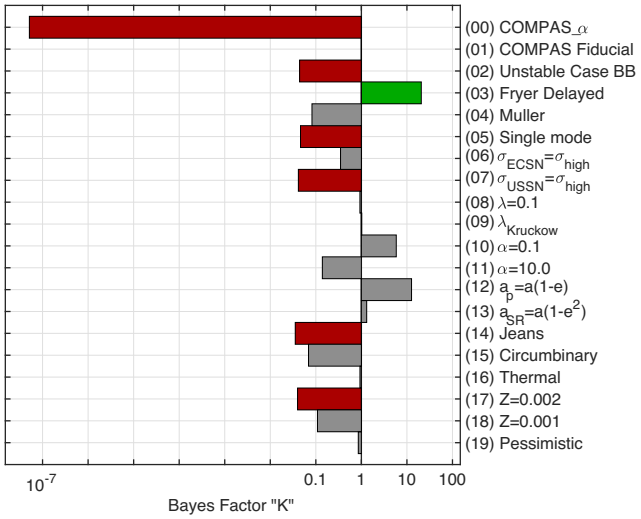

Figure 1. The ratio of the likelihood of each model to the likelihood of the `Fiducial` model (01). Green (red) bars denote models significantly favoured (disfavoured) by an odds ratio of greater than 20 : 1 relative to the `Fiducial` model.

2.3 Model comparison

In order to quantify how well our models match the observed Galactic DNS period–eccentricity (P–e) distribution, we calculate the likelihood $\mathcal{L}_i$ that observations could have come from the synthesized DNS population for each model i. We use the P–e distribution because all 14 observed Galactic DNSs (cf. Table 1) have precise measurements of the period and the eccentricity, but only half of them have precise measurements of their individual masses. We do not use any of the mass measurements in the likelihood calculation. We also do not attempt to account for selection biases in the observed P–e distribution.

The details of how the likelihoods $\mathcal{L}_i$ are computed are given in Appendix A. We quote our results as the ratio of the likelihood for a given model to the likelihood of the `Fiducial` model i, that is, we define the Bayes factor $\mathcal{K}_i$ as

$$\log \mathcal{K}_i = \log \mathcal{L}_i - \log \mathcal{L}_{01}, \quad (1)$$

where all logarithms in this study are base e unless stated otherwise. A positive log Bayes factor $\log \mathcal{K} > 0$ means that the given model is preferred over the `Fiducial` model. On the other hand, a negative log Bayes factor means that the `Fiducial` model is preferred over the given model. If all models have equal priori probabilities, the odds ratio is equal to the Bayes factor. The odds ratio determines how significantly favoured or unfavoured the model is with respect to the `Fiducial` model; for an introduction to Bayesian analysis, see Jaynes et al. (2003) and Sivia (1996). For readers unfamiliar with Bayes factors, we also indicate when odd ratios for these model comparisons exceed 20 : 1 (or 1 : 20 for disfavoured models), loosely corresponding to the common significance threshold with a p-value of $p < 0.05$. Limited sampling of the synthetic distributions leads to uncertainties of order unity on $\log \mathcal{K}_i$, corresponding to a factor of 2 or 3 uncertainty in the Bayes factor; this statistical uncertainty can be improved with longer simulations. The Bayes factors calculated for our models are plotted in Fig. 1 and presented in Table 2.

Table 2. We list all simulations computed for this study; for simulations (02) through (19), we state the physical interaction or assumption varied relative to the `Fiducial` model and the actual parameter varied. For each simulation, we give the formation rate $\mathcal{R}$ of DNS that will merge in a Hubble time in the Galaxy, its log Bayes factor relative to the `Fiducial` model (see Appendix A) given the observed Galactic DNS P–e distribution and the fraction f of formed DNSs that merge within a Hubble time. See Fig. A1 for the predicted P–e distributions for all models.

Number	Physics	Variation	$\mathcal{R}$ (Myr^{-1})	log($\mathcal{K}$)	f
00	COMPAS_α		11.34	− 16.78	0.61
01	COMPAS `Fiducial`		24.04	0	0.73
02	Stability	Case BB: unstable	24.54	− 3.12	0.94
03	SNe	Fryer delayed	28.05	3.03	0.76
04	SNe	Müller	30.95	− 2.50	0.87
05	SNe	Single mode	9.16	− 3.08	0.83
06	SNe	$\sigma_{\rm ECSN} = \sigma_{\rm high}$	15.11	− 1.05	0.77
07	SNe	$\sigma_{\rm USSN} = \sigma_{\rm high}$	13.53	− 3.19	0.81
08	CE	$\lambda = 0.1$	16.30	− 0.07	0.85
09	CE	$\lambda_{\rm Kruckow} \propto R^{-5/6}$	9.08	0.02	0.84
10	CE	$\alpha = 0.1$	5.26	1.76	0.59
11	CE	$\alpha = 10.0$	9.54	− 1.97	0.36
12	Circularization	$a_{\rm p} = a(1-e)$	14.14	2.54	0.77
13	Circularization	$a_{\rm SR} = a(1-e^2)$	15.31	0.27	0.72
14	Mass-loss mode	Jeans	6.69	− 3.34	0.21
15	Mass-loss mode	Circumbinary	28.05	− 2.67	0.94
16	Distribution	$f_e(e)$ = thermal	10.22	− 0.07	0.69
17	Metallicity	$Z = 0.002$	20.09	− 3.23	0.71
18	Metallicity	$Z = 0.001$	24.06	− 2.22	0.72
19	CE	Pessimistic	14.29	− 0.16	0.70

3 RESULTS

We evolve 10^6 binaries[2] with initial metallicity $Z_\odot = 0.0142$. Although Galactic NSs were born at a range of metallicities, we use solar metallicity values (Asplund et al. 2009) for bulk composition as a proxy for ongoing star formation metallicity in the Galaxy.

We present the detailed results of our `Fiducial` model (01)[3] and some variations to it, all with identical initial parameters (unless stated otherwise). The diagnostic tools we use to analyse all of our variations is the P–e distribution (see Fig. 2 and Section 2.3, as well as Appendix A for details), remnant NS mass distribution (see Fig. 7) and formation rate estimates (see Table 2). We report the number of significant figures based on statistical simulation uncertainty, i.e. the Monte Carlo uncertainty.

We illustrate the plausible distribution of simulated Galactic DNSs (see Fig. 2 for `Fiducial` model and Fig. A1 for all models), which shows, in the P–e plane, how systems may evolve from DNS formation to a typical observable distribution. To illustrate this, we assign each binary a random probability of being born at any given point in the last 10 Gyr (a proxy for the age of the Galactic thin disc, see del Peloso et al. 2005), and then follow their gravitational-wave-driven orbital evolution until present time.

Our models predict the mass ratio distribution (Fig. 3) and time distributions (Fig. 4). The mass ratio distribution depends on the explosion mechanism of the SNe. The time distributions describe the formation time ($t_{\rm form}$), coalescence time ($t_{\rm c}$), and delay time ($t_{\rm delay}$). The formation time is the time it takes a binary to evolve from ZAMS to DCO formation. The coalescence time is the time it takes that DCO to inspiral until coalescence due to gravitational radiation, following the post-Newtonian approximation as given by Peters (1964). The delay time is the sum of the formation time and the coalescence time.

Given the orbital properties of the population and the estimated time distributions we are able to predict the formation rate $\mathcal{R}$ of DNSs that will merge in a Hubble time (assuming $H_0^{-1} = 14.03$ Gyr in a flat ΛCDM cosmology; Planck Collaboration XIII 2016). If a system has a delay time of less than a Hubble time we include it in the formation rate $\mathcal{R}$.

Formation rates are calculated for a galaxy with a continuous star formation rate of $f_{\rm SFR} = 2.0\,{\rm M}_\odot\,{\rm yr}^{-1}$, with all systems in our simulated universe born in binaries.[4] The star formation rate is chosen to mimic the Milky Way value of $f_{\rm SFR} = 1.9 \pm 0.4\,{\rm M}_\odot\,{\rm yr}^{-1}$ (Chomiuk & Povich 2011); any shifts in the chosen value would proportionately shift the quoted DNS formation rate.

A summary of all the formation rates and Bayes factors for the different variations is given in Table 2.

3.1 On the `Fiducial` model

3.1.1 Formation channels

There are two main ways that DNSs can form in our `Fiducial` model. We call these two dominant channels – *Channel I* and *Channel II*; some variations on these channels with additional mass transfer episodes or a different sequential order are possible. Below we will explain the crucial steps in these formation channels, mentioning the fraction of systems that went through different stages of binary evolution. We find that 0.13 per cent of all simulated binaries become DNSs.

[2]The total mass of evolved binaries is 20 250 000 $\rm M_\odot$ for each simulation; this represents 78 587 000 $\rm M_\odot$ of total star-forming mass under the assumed initial mass distribution. The results of all simulations can be found in: http://www.sr.bham.ac.uk/compas/data/GalacticDNSs/

[3]We will label the variations by their number (see Table 2) in parentheses; e.g. `Fiducial` model (01) or COMPAS$_\alpha$ (00).

[4]While our models only include binaries, our orbital period distribution allows wide systems to evolve effectively as single stars. In fact, we find that more than half of our simulated binaries never engage in mass transfer.

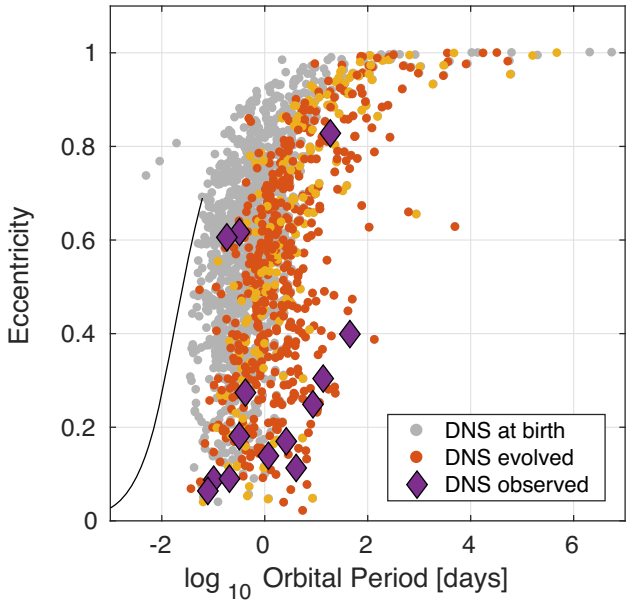

Figure 2. Predicted *P*–*e* distribution of Galactic DNSs under the `Fiducial` model. Grey dots are all DNSs at DCO formation. DCO period and eccentricity are evolved forwards from birth until present age given gravitational-wave radiation, removing a fraction of the short-lived short-period binaries from the observable population. Coloured dots represent the DNS distribution at present age. Colour denotes the type of CE phase: red for a single core, in which only the donor has a clear core-envelope separation, and yellow for a double-core CE phase, in which both the donor and the accretor have a clear core-envelope separation. The single-core and double-core CE phases can be, in most cases, associated with *Channel I* and *Channel II,* respectively (see Section 3.1.1; Figs 5 and 6 for more details). *Channel I* and *Channel II* are the first and second most common formation channels, respectively. Purple diamonds represent the observed Galactic DNSs; all observed systems have precise *P*–*e* measurements with error bars within the thickness of the symbol. The black curve illustrates a gravitational-wave-driven *P*–*e* evolution from DCO formation to merger; this system, with initial $P = 1.5$ h, $e = 0.69$, and characteristic NS masses $m_1 = m_2 = 1.2\,\mathrm{M}_\odot$, would merge in ≈3 Myr through gravitational-wave emission.

Channel I, illustrated in Fig. 5, is responsible for the formation of roughly 70 per cent of all DNSs. This formation channel is consistent with the canonical channel described by Bhattacharya & van den Heuvel (1991) and Tauris & van den Heuvel (2006). *Channel I* involves a single-core CE phase in which the primary has already collapsed into an NS. A single-core CE phase occurs when only one of the stars has a clear core-envelope separation; all compact objects are assumed not to have a clear core-envelope separation, as well as MS and HeMS stars. This channel proceeds as follows:

Channel I:

(i) The two stars begin their evolution with the more massive one (the primary) evolving faster than its companion.

(ii) ≈22 per cent of the all the initial systems experience stable mass transfer from the primary during the HG phase on to an MS secondary. This is because 52 per cent of the primaries never expand enough to start the mass transfer, and of the ones that do 47 per cent are stable during this phase ($0.48 \times 0.47 \approx 0.22$).

(iii) ≈4 per cent of those ≈22 per cent systems contain a primary that experiences an SN explosion producing an NS and remaining in a bound orbit. In the mass transfer episode, the primary becomes an HeMS star. The majority of the HeMS stars are either too light to become NSs or heavy enough to become BHs. Only 30 per cent of them have the mass of an NS progenitor. In this first SN explosion, there are 10 times more CCSNe than there are ECSNe, but given the higher natal kick magnitude, their survival rate is only 9 per cent compared to 47 per cent of the ECSNe.

(iv) ≈25 per cent of those ≈4 per cent systems experience and survive a CE phase initiated by the post-MS secondary. Only 33 per cent of the secondaries expand enough to engage into an RLOF mass transfer. This second mass transfer episode, with a primary NS accretor, is usually dynamically unstable and leads to a CE phase. 85 per cent of these systems are able to successfully eject their envelope, hardening the binary by two or three orders of magnitude.

(v) ≈40 per cent of those ≈25 per cent systems begin a third mass transfer episode (case BB) of a HeHG secondary on to an NS primary. There the HeHG star recycles its NS companion while being stripped for a second time until a CO core (we call this ultra-stripped, see Section 2.2.3). Half of those cores are in the right mass range to become an NS (lighter cores may form an NS–white dwarf binary while heavier cores yield an NS–BH binary).

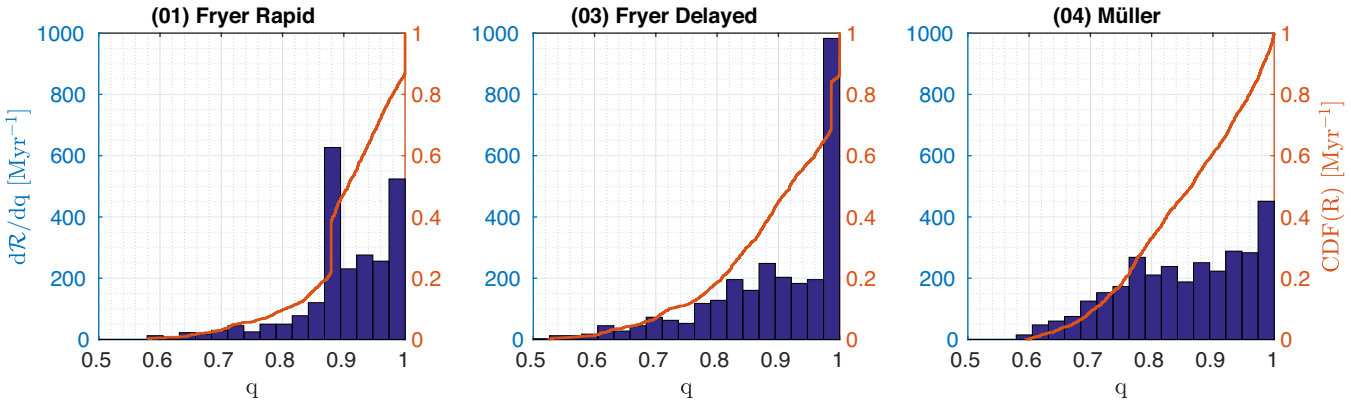

Figure 3. Mass ratio distribution of merging DNSs (blue histogram) and its cumulative distribution function (orange curve) for three SN fallback and natal kick models: (01) Fryer Rapid (left), (03) Fryer Delayed (middle), and (04) Müller (right). See Sections 3.1.2 and 3.3 for a discussion of the evolutionary channels leading to sharp features in the histograms.

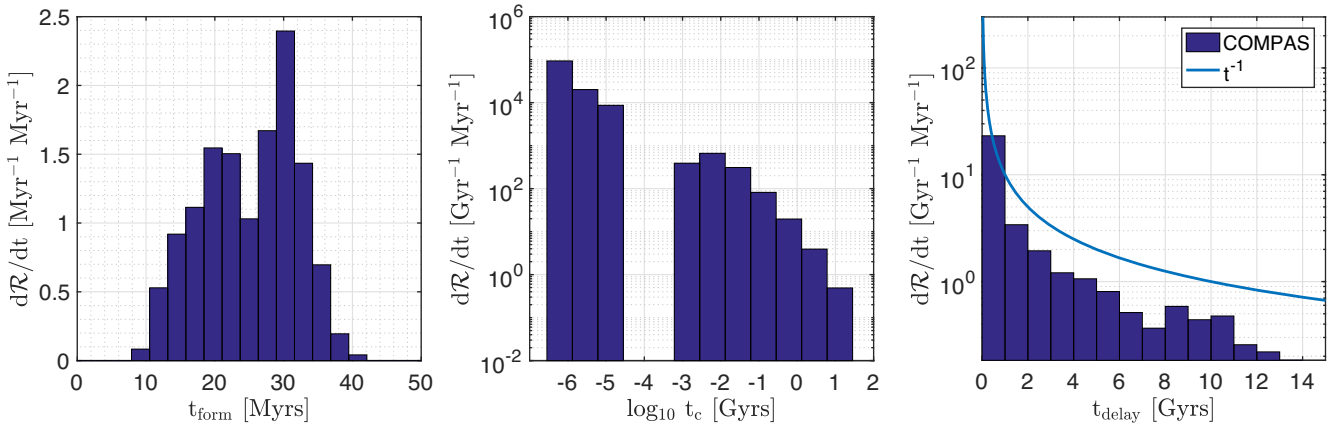

Figure 4. Time distributions or merging DNSs (blue histogram) for our `Fiducial` model (01): time t_{form} from ZAMS to DNS formation (left), coalescence time t_c from DNS formation to merger (middle), and total delay time t_{delay} from ZAMS to merger (right). We show a $d\mathcal{R}/dt \propto t_{delay}^{-1}$ curve for comparison with the delay time distribution in the right panel. The apparent gap in the middle panel is a sampling artefact.

(vi) ≈96 per cent of those ≈40 per cent systems will remain bound after the second SN explosion and form a DNS. The tight post-CE orbit and the reduced natal kicks for USSNe make it relatively easy for binaries to survive the natal kick and form a DNS system. The systems that are disrupted either lost enough mass and/or had orbital velocities low enough that even the reduced USSN natal kick disrupts the system.

The secondary formation *Channel II*, illustrated in Fig. 6, is responsible for forming approximately 21 per cent of DNSs; it is prevalent for systems with initial mass ratio $q_{ZAMS} \approx 1$ and, therefore, similar evolutionary time-scales of both stars in the binary. This channel experiences a double-core CE phase (Brown 1995; Dewi, Podsiadlowski & Sena 2006; Hwang et al. 2015), in which both of the stars have a clear core-envelope separation, before the first SN. *Channel II* proceeds as follows:

Channel II:

(i) Again, the two stars begin their evolution with the primary evolving faster than its companion.

(ii) ≈1 per cent of the primaries start their first mass transfer episode as either a CHeB or an EAGB star with a secondary that is a slightly less evolved HG or a CHeB star. Almost all of these systems (90 per cent) initiate a double-core CE phase during this mass transfer episode.

(iii) ≈35 per cent of those ≈1 per cent binaries can eject their envelopes. Only a tiny fraction (≈2 per cent) lose enough mass to become white dwarfs, whereas the majority become two HeMS stars in a tighter orbit.

(iv) ≈87 per cent of those ≈35 per cent systems have primaries that can initiate a second mass transfer episode (case BB). The primaries donate their helium envelope to the secondary HeMS star. All these episodes are dynamically stable.

(v) ≈35 per cent of those ≈87 per cent systems are able to have a primary experience an SN explosion producing an NS and remaining in a bound orbit. As in *Channel I*, the mass transfer episodes reduce the masses of the primary and only 63 per cent can experience an SN explosion. They are all CCSNe and although the CE phase leaves them in a tight orbit the higher natal kick magnitude still disrupts 45 per cent of these systems.

(vi) ≈80 per cent of those ≈35 per cent systems begin a third mass transfer episode (case BB) from the secondary to an NS accretor. This mass transfer episode on to the NS is defined to always be stable and the secondary now becomes an ultra-stripped CO core.

(vii) ≈55 per cent of those ≈80 per cent systems have secondaries that experience and survive an SN explosion and become NSs. 71 per cent of the CO cores are massive enough to explode as an SN, and given the previous episode of mass transfer they are all USSNe. The lower natal kicks and tighter orbits help to get a survival rate of 77 per cent, leaving a DNS system behind.

All simulated DNS systems are shown in the *P*–*e* distributions in Figs 2 and 8 and in Appendix A. Most of the DNS systems that survived a single-core CE phase come from *Channel I*, while most of those that survived a double-core CE phase come from *Channel II*. The rest of the DNSs, about 9 per cent of the total, come from more exotic or fortuitous channels, including non-recycled DNSs (≤1 per cent of all Galactic-like DNSs). Non-recycled DNS progenitors are systems that never had stable mass transfer on to an NS (Belczyński & Kalogera 2001), which leads to spin up and recycling; all of them experienced CEs in our models, which we assume to be inefficient at spinning up the NS and suppressing its magnetic field (MacLeod & Ramirez-Ruiz 2015).

We find that our `Fiducial` model has a formation rate of $\mathcal{R} = 24.04$ per Milky Way equivalent galaxy per Myr. All of our DNSs experience and survive at least one CE phase, 23 per cent of them in a double-core scenario.

3.1.2 *Mass ratio distribution*

Fig. 7 shows the mass distribution of all the Galactic DNSs at the moment of birth, while Fig. 3 shows the distribution of the predicted mass ratio q_{DCO} for the merging Galactic DNSs. We define $q_{DCO} = m_{NS,lighter}/m_{NS,heavier}$; the heavier NS is not necessarily the more massive star at ZAMS. In the `Fiducial` model, the initially less massive star produces the more massive NS in 31 per cent of the systems, due to the accretion of mass from the companion, and its core growth, during the early phases of evolution. The mass ratio of these systems lies between $0.58 \leq q_{DCO} \leq 1$. Among the merging Galactic DNSs, 90 per cent of the systems have $q_{DCO} > 0.8$, 50 per cent have $q_{DCO} > 0.9$ and 30 per cent have $q_{DCO} > 0.95$. There are two significant peaks in this distribution: (i) the first peak, with ≈16 per cent of systems have $q_{DCO} \approx 0.88$; most

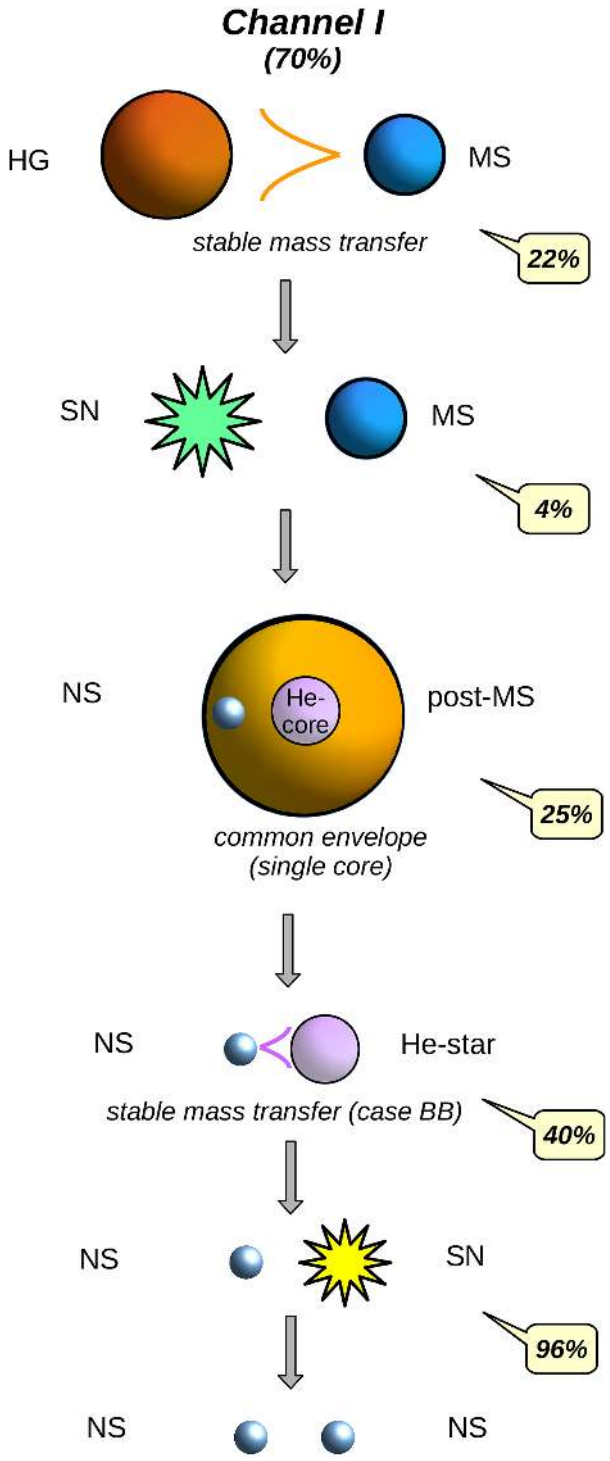

Figure 5. Evolutionary history of formation *Channel I* (top to bottom); 70 per cent of all DNSs in our `Fiducial` population were formed through this channel. The numbers in the call-out symbols represent the per centage of simulated binaries that end up in that particular stage among those that follow the preceding evolutionary history. For example, 22 per cent of all simulated binaries experience stable mass transfer from a HG primary on to an MS secondary; among those 22 per cent, 4 per cent of systems will have a primary that undergoes an SN producing an NS, while remaining in a bound orbit, and so on.

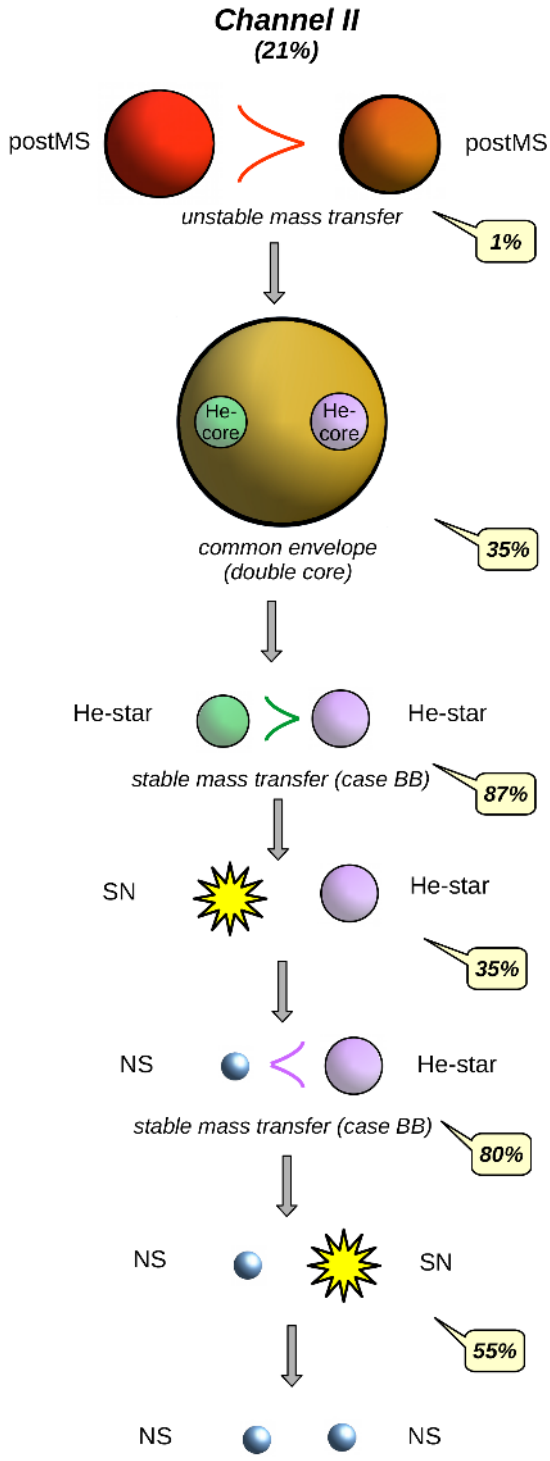

Figure 6. Evolutionary history of formation *Channel II* (top to bottom); 21 per cent of all DNSs in our `Fiducial` population were formed through this channel. The numbers in the call-out symbols represent the per centage of simulated binaries that end up in that particular stage among those that follow the preceding evolutionary history. For example, 1 per cent of all simulated binaries initiate mass transfer, while both companions are post-MS stars; among those 1 per cent, 35 per cent enter and survive a double-core CE phase, and so on.

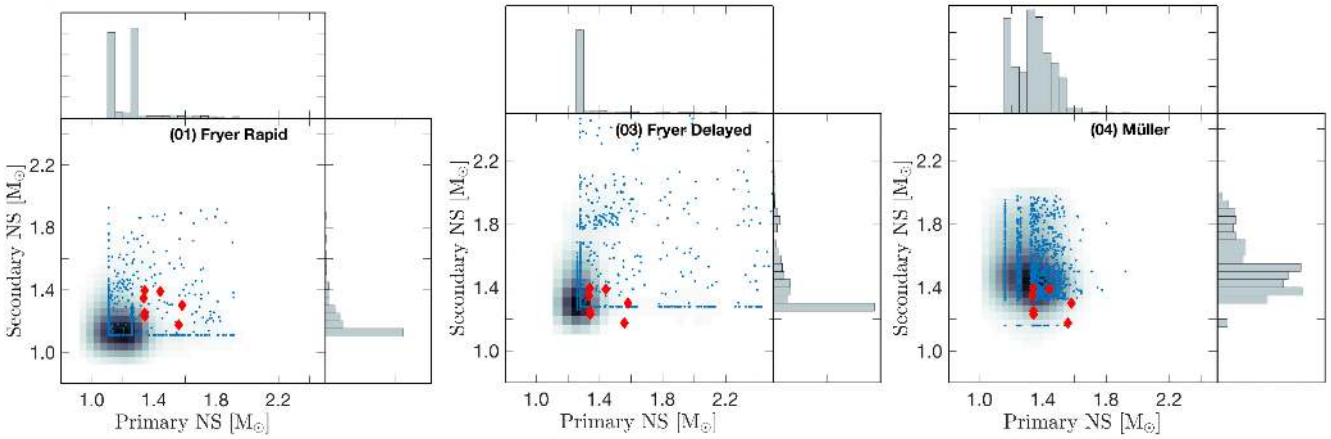

Figure 7. Predicted mass distribution of all predicted DNSs under three different SN fallback and natal kick models: (01) Fryer Rapid (left), (03) Fryer delayed (centre), (04) Müller (right). Primary and secondary masses of the NSs are shown in the horizontal and vertical axes, respectively. Red diamonds denote the observed Galactic DNSs with well-constrained masses (see Table 1), with pulsar and companion NS masses shown in the horizontal and vertical axes, respectively. Blue dots correspond to the DNS masses at DCO formation. The density map shows the 2D DNS mass probability distribution; the histograms show its 1D linear projections. See Sections 3.1.2 and 3.3 for a discussion of the evolutionary channels leading to sharp features in the histograms.

systems close to this mass ratio are formed through *Channel I*, with their first NS being an ECSN (with gravitational mass of $1.26\,M_\odot$) and the second an USSN (with lower mass remnants of $1.1\,M_\odot$), (ii) the second peak, with ≈14 per cent of the total DNSs, has a mass ratio $q_{\rm DCO} \approx 1$, from $q_{\rm ZAMS} \approx 1$ systems that evolved through the double-core CE, with a low mass CCSN and an USSN (i.e. *Channel II*). The mass range of NSs in our `Fiducial` population is $[m_{\rm NS,min}, m_{\rm NS,max}] = [1.1, 1.9]\,M_\odot$.

3.1.3 *Time distributions*

We define the following time-scales: (i) formation time $t_{\rm form}$ as the time from ZAMS to DCO formation, (ii) coalescence time $t_{\rm c}$ as the time from DCO formation to merger, (iii) total delay time $t_{\rm delay}$ as the time from ZAMS to merger. Fig. 4 shows the distributions for $t_{\rm form}$, $t_{\rm c}$, and $t_{\rm delay}$ for our `Fiducial` model. Time distributions were made based on only those DNSs that have a merger time of less than the Hubble time. The extreme ends of the time distributions are systems with $8.5 \leq t_{\rm form}\,{\rm Myr}^{-1} \leq 41.6$, $900.0 \leq t_{\rm c}\,{\rm yr}^{-1}$, and $12.6 \leq t_{\rm delay}\,{\rm Myr}^{-1}$.

Fewer than 0.5 per cent of merging DNSs have very short coalescence times of less than 10 Myr (see the middle panel of Fig. 4 and outliers in Fig. C1 – note that the apparent gap in the middle panel is a sampling artefact, and does not represent an actual gap in the population). These systems usually experience CEs, reduce their orbit during case BB mass transfer and have fortuitous natal kick directions that place them on a low-periapsis orbit at DCO formation. Systems with $t_{\rm c} > 10^{-3}$ Gyr represent the bulk of the population in Fig. 2; shorter coalescence times are exhibited by outliers with orbital periods of $\lesssim 10^{-2}$ d.

3.1.4 *Supernovae*

Of all the NSs in DNS systems, 20 per cent were formed via ECSNe. 92 per cent of the initially less massive secondaries in these DNSs experienced ultra-stripping before exploding. Only 0.1 per cent of the DNS systems had both stars experiencing an ECSN. In 19 per cent of the DNSs the primary went through an ECSN and was later recycled by case BB mass transfer from the secondary. The secondary is stripped by this mass transfer and explodes in an USSN.

In our single stellar models at $Z = Z_\odot$, ECSN progenitors have masses at ZAMS of $7.8 \leq m/M_\odot \leq 8.1$; more recent detailed models find that the mass range of single star progenitors at metallicity $Z = 0.02$ that explode as an ECSN is $7.5 \leq m/M_\odot \leq 9.25$ (Poelarends et al. 2008). Interaction during binary evolution increases this range to $7.8 \leq m_1/M_\odot \leq 28.4$ for the primary and $4.5 \leq m_2/M_\odot \leq 10.8$ for the secondary in our study. Detailed studies of ECSNe from interacting binary systems find that the mass range for an interacting primary at $Z = 0.02$ is between $13.5 \leq m/M_\odot \leq 17.6$ (Poelarends et al. 2017), where $17.6\,M_\odot$ is the highest mass primary used in that study.

Metallicity does not play a strong role in modifying the NS mass range. We explore lower metallicity populations at $Z = 0.002$ (17) and $Z = 0.001$ (18), and find that, for single stars, the ECSN progenitor masses at ZAMS decrease to $7.0 \leq m/M_\odot \leq 7.2$ and $6.6 \leq m/M_\odot \leq 6.9$, respectively. However, the remnant mass from an ECSN does not vary as a function of metallicity and is always fixed to be $m_{\rm ECSN} = 1.26\,M_\odot$. Furthermore, our minimum and maximum NS masses of $[m_{\rm NS,min}, m_{\rm NS,max}] = [1.1, 1.9]\,M_\odot$ do not change as a function of metallicity.

3.2 Variations

COMPAS is a modular code designed to explore the effects of different treatments of uncertain physical assumptions. Given the complexity of the formation channels, we explore the uncertainties by changing one assumption per variation. This allows us to link all the changes in the population and its formation channels to a specific physical treatment and test the robustness of our `Fiducial` model. The parameters of the physical interactions may be correlated; since computing these correlations is computationally expensive (see e.g. Barrett et al. 2018), we do not consider them here.

3.2.1 *On mass transfer stability criteria*

Stable case BB mass transfer leads to orbital periods similar to the observed Galactic DNS population. Meanwhile, unstable case

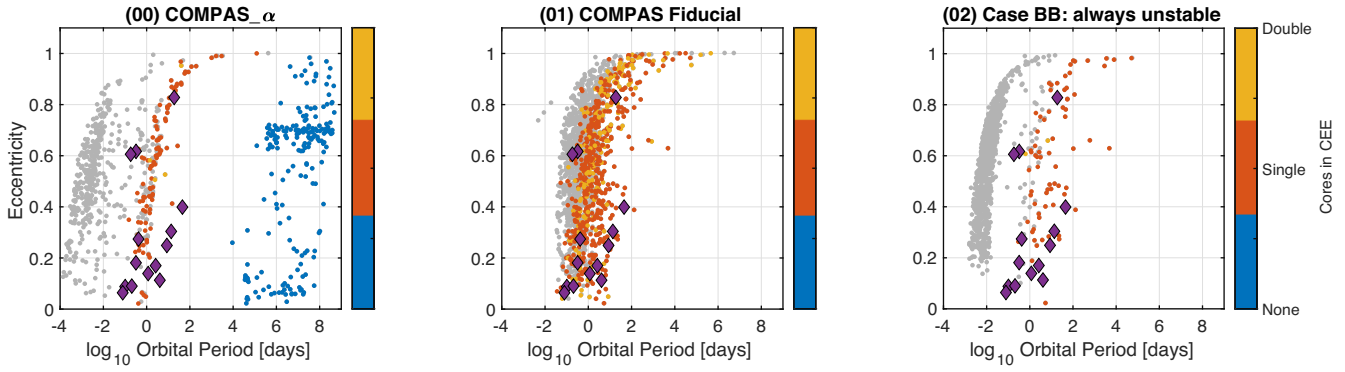

Figure 8. Predicted *P*–*e* distribution of Galactic DNSs at DCO formation: (00) Stevenson et al. (2017) standard (left), (01) `Fiducial` (middle), (02) variation with unstable case BB mass transfer (right) (for more details, see Table 1). Purple diamonds represent the Galactic DNSs. Colour denotes the type of CE phase: blue for no CE phase, red for a single core, and yellow for a double-core CE phase. The single-core and double-core CE formations are typically associated with *Channel I* and *Channel II*, respectively. Blue dots on the left-hand panel correspond to double-ECSNe with $\sigma_{\rm ECSN} = 0\,{\rm km\,s^{-1}}$ in COMPAS_α.

BB, leading to a CE phase, typically results in sub-hour orbital periods (see the right-hand panel of Fig. 8); such orbital periods yield coalescence times of $\lesssim$10 Myr. About 90 per cent of Galactic DNS progenitors in the `Fiducial` model experience case BB mass transfer. At the onset of the episode, 90 per cent of systems have mass ratio $q \geq 0.2$ and 9 per cent with $q \geq 0.4$. Claeys et al. (2014) assume that mass transfer of HeHG donors with a degenerate accretor will be stable if $q > 0.21$ (see table 2 of that paper), while Tauris et al. (2015) propose to consider mass ratio and orbital period to define stability criteria in order to account for the evolutionary phase of the donor at the onset of RLOF; in that study, orbital periods of $P \geq 0.07$ d at the onset of RLOF lead to stable case BB mass transfer. In our `Fiducial` model, all Galactic DNS progenitors have $P \geq 0.07$ d at the onset of case BB mass transfer.

In COMPAS, we probe the extreme cases of either stable or dynamically unstable case BB mass transfer for a whole population. The difference in formation rate $\mathcal{R}$ between the stable (01) and dynamically unstable (02) case BB mass transfer is comparable within a few per cent, with $\{\mathcal{R}_{01},\mathcal{R}_{02}\} = \{24.04, 24.54\}$ per Galaxy per Myr. Nevertheless, the log Bayes factor of model (02) relative to model (01) is $\log \mathcal{K} = -3.12$, which favours our `Fiducial` model, and ultimately, significantly favours stable against unstable mass transfer in a dichotomous scenario. In our `Fiducial` population, the assumption of case BB mass transfer being always stable is in broad agreement with mass ratio constraints from Claeys et al. (2014), which would result in more than 90 per cent of these systems experiencing stable mass transfer. If instead we used the stability criteria presented in Tauris et al. (2015) (as shown in Kruckow et al. 2018), all of the aforementioned systems would experience stable mass transfer.

3.2.2 *On the 'delayed' explosion scenario*

To test the effect of the explosion mechanism on our predictions, we investigate three prescriptions; one being the 'rapid' (01) explosion mechanism as presented in our `Fiducial` model (see Section 3.1.4). The second one is the 'delayed' (03) explosion mechanism applied in our model (03) and to be explained below, while the third is the 'Müller' (04) prescription presented in Section 3.2.4.

The 'delayed' explosion mechanism proposed in Fryer et al. (2012) allows for accretion on to the proto-NS before the standing-accretion shock instability or convection become powerful enough to support a neutrino-driven explosion. This accretion removes the mass gap and creates a continuous remnant mass distribution from NS to BH. This continuous distribution of compact-object remnant masses requires us to define an arbitrary mass cut to distinguish NSs from BHs; we follow Fryer et al. (2012) and set this mass cut to 2.5 $M_\odot$, which is higher than the maximum mass of 2.0 $M_\odot$ from the other explosion mechanisms used in this study.

The 'delayed' explosion mechanism formation rate is $\mathcal{R} = 28.05$ per Milky Way equivalent galaxy per Myr. The 'delayed' explosion mechanism, which changes the remnant mass given a CO core at the moment of an SN, produces a slightly different *P*–*e* distribution than the 'rapid' explosion mechanism because of the impact of mass-loss at the moment of the explosion on the binary's orbit. The middle panel of Fig. 7 shows that the 'delayed' explosion mechanism lies close to the observed population and is preferred over the 'rapid' explosions mechanism in the `Fiducial` model with a $\log \mathcal{K} = 3.03$. The 'delayed' explosion scenario, which does not have a mass gap between NSs and BHs, has the largest likelihood of all models.

3.2.3 *On the SN kick distribution and magnitude*

Both mass-loss during an SN and the natal kick magnitude and direction modify the orbital parameters and determine whether the binary is disrupted. Low natal kick ECSNe and USSNe therefore play a prominent role in DNS formation and possible eventual merger, as would low-mass iron-core-collapse SNe with a reduced natal kick. Our modelling allows for testing a bimodal natal kick distribution, which distinguishes between CCSNe (high mode, $\sigma_{\rm high} = 265\,{\rm km\,s^{-1}}$), ECSNe (low mode, $\sigma_{\rm low} = 30\,{\rm km\,s^{-1}}$), and USSNe (low mode). When allowing for a bimodal distribution, but with only USSN (06) or ECSN (07) contributing to the low component of the Maxwellian distribution, the DNS formation rate $\mathcal{R}$ drops by a factor of $\approx$2 relative to the `Fiducial` model. We also simulated a single high-mode distribution (05) with high natal kicks for both USSNe and ECSNe, which is also the assumption in COMPAS_α (00). In this case, $\mathcal{R}$ decreases by a factor of $\approx$3; this single high-mode variation (05) also fails to create the observed longer period DNSs with low eccentricities. The formation rates and log Bayes factors are $\{\mathcal{R}_{05}, \mathcal{R}_{06}, \mathcal{R}_{07}\} = \{9.16, 15.11, 13.53\}$ per Milky Way equivalent galaxy per Myr and $\log\{\mathcal{K}_{05}, \mathcal{K}_{06}, \mathcal{K}_{07}\} = \{-3.08, -1.05, -3.19\}$ for variations with a single high mode (05), $\sigma_{\rm ECSN} = \sigma_{\rm high}$ (06) and $\sigma_{\rm USSN} = \sigma_{\rm high}$ (07), respectively. Given the log Bayes factors,

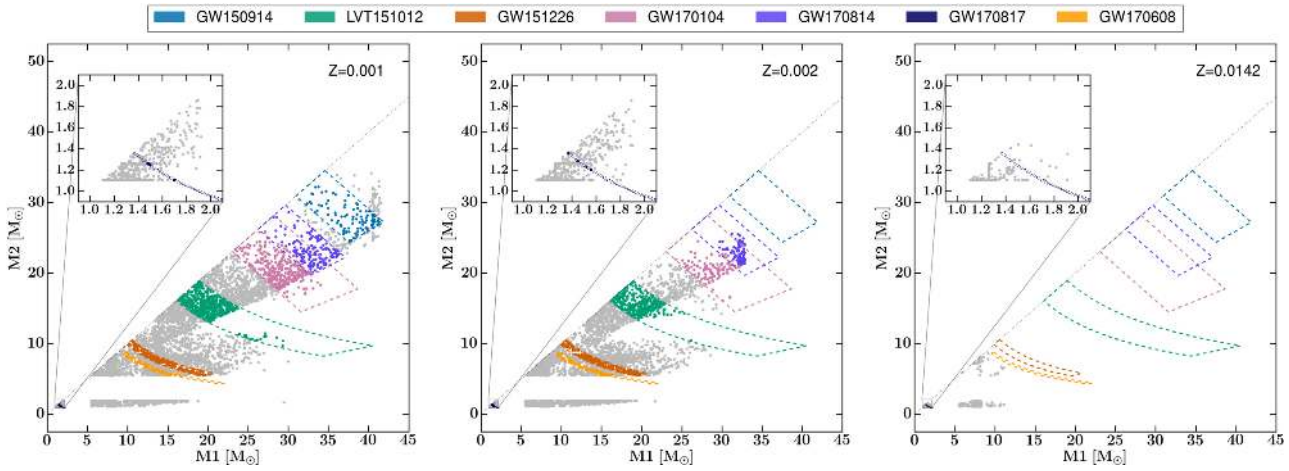

Figure 9. Masses of merging compact binaries predicted by the `Fiducial` model at three different metallicities: $Z = 0.001$ (left), $Z = 0.002$ (centre) (cf. Stevenson et al. 2017), and solar metallicity $Z = 0.0142$ (right). Coloured regions correspond to masses matching advanced LIGO detections within the reported 90 per cent credible intervals.

the `Fiducial` model is significantly preferred over single high mode (05) and $\sigma_{\rm USSN} = \sigma_{\rm high}$ (07) variations. It is preferred, but not significantly, over the $\sigma_{\rm ECSN} = \sigma_{\rm high}$ (06) variation.

3.2.4 *On the Müller prescription*

We introduce the 'Müller' (04) explosion prescription as fitting formulae to the detailed models described by Müller et al. (2016). The full description and fitting formulae are provided in Appendix B for use in other population synthesis studies. The 'Müller' prescription maps a CO-core mass to an NS remnant mass and a natal kick. The remnant and ejecta mass and the explosion energy are obtained semi-analytically and calibrated to numerical models. We update the analytic SN models of Müller et al. (2016) by using a shock radius factor $\alpha_{\rm turb} = 1.18$ and a compression ratio at the shock $\beta = 3.2$, which fit constraints on the progenitor masses of type IIP supernovae (Smartt 2015) slightly better than the original version. The natal kick velocity is obtained from these by assuming a uniform ejecta anisotropy (Janka 2017). The natal kick magnitude, with a dominant mode at $v_{\rm kick} \approx 100\,{\rm km\,s^{-1}}$ is therefore correlated with the NS remnant mass, unlike for the other models considered here. The mass range of NSs in our evolved population, using the 'Müller' explosion mechanism, is $[m_{\rm NS,min}, m_{\rm NS,max}] = [1.2, 2.0]\,{\rm M}_\odot$. The formation rate and log Bayes factor of model (04) are $\mathcal{R} = 30.95$ per Milky Way equivalent galaxy per Myr and $\log \mathcal{K} = -2.50$. This Bayes factor was calculated using only the *P*–*e* distribution. The mass distribution (Figs 7 and 10) will play an important role in distinguishing the 'rapid' (01), 'delayed' (03), and 'Müller' (04) explosion mechanism variations.

3.2.5 *On the comparison with* COMPAS_α

Here, we compare our `Fiducial` model to the one described by Stevenson et al. (2017, (00), COMPAS_α). The latter uses different parametrizations: both CCSNe and USSNe natal kicks are drawn from a high-mode Maxwellian distribution and all ECSNe have a $v_{\rm kick} = 0\,{\rm km\,s^{-1}}$; stability is determined using $\zeta_{\rm SPH}$ for all stellar phases, which often leads to dynamically unstable mass transfer, particularly during case BB RLOF; and the binding energy parameter is $\lambda_{\rm fixed} = 0.1$ for all stars in any evolutionary stage.

That study was successful in explaining all gravitational-wave events from the first advanced LIGO observing run (GW150914, LVT151012, and GW151226; Abbott et al. 2016b,a,c) via a single evolutionary scenario: isolated binary evolution. However, the same assumptions fail to reproduce the observed Galactic DNS populations (see the left-hand panel of Fig. 8). COMPAS_α (00), which yields a DNS formation rate of $\mathcal{R}_{00} = 11.34$ per Milky Way equivalent galaxy per Myr, is the least preferred model from our variations, with a log Bayes factor of $\log \mathcal{K} = -16.78$. In particular, the extreme hardening of case BB binaries through a second CE phase in COMPAS_α leads to a gap in the *P*–*e* distribution, where systems such as J0737–3039 are observed. From the major changes, dynamical stability during case BB mass transfer and a bimodal natal kick distribution are preferred over the alternatives in the `Fiducial` model [see unstable case BB mass transfer (02) and single mode natal kick distribution (05) variations], which are ruled out in our model comparison.

On the other hand, the `Fiducial` model is able to explain, in a consistent form with Stevenson et al. (2017), the gravitational-wave events from the first advanced LIGO observing run, as well as GW170104 (Abbott et al. 2017a), GW170608 (The LIGO Scientific Collaboration et al. 2017), GW170814 (Abbott et al. 2017b), and the DNS merger GW170817 (Abbott et al. 2017c), all detected during the second observing run of advanced LIGO and advanced Virgo (see Fig. 9).

3.2.6 *On the circularization during mass transfer*

Our `Fiducial` model does not circularize the orbit during a mass transfer episode, except as a consequence of dynamically unstable mass transfer (CE). As a variation, we consider circularization at the onset of RLOF (e.g. as a consequence of tidal dissipation prior to mass transfer or during the episode). We allow for two types of circularization: (i) circularization to periastron $a_p = a(1 - e)$, which dissipates both orbital energy and angular momentum (12), (ii) circularization to semilatus rectum $a_{\rm SR} = a(1 - e^2)$, which conserves the angular momentum of the orbit (13). The DNS formation rates and log Bayes factors are $\{\mathcal{R}_{12}, \mathcal{R}_{13}\} = \{14.14, 15.31\}$ per Milky Way equivalent galaxy per Myr and $\log\{\mathcal{K}_{12}, \mathcal{K}_{13}\} = \{2.54, 0.27\}$, respectively. Rates decrease by less than a factor of 2. Circularization

to periastron at the onset of mass transfer is slightly preferred than the alternatives, but not enough for us to consider it clearly preferred over the `Fiducial` model. Circularization that conserves angular momentum is not favoured nor disfavoured with respect to the `Fiducial` assumption (i.e. no circularization at all).

3.2.7 On the angular-momentum loss during non-conservative mass transfer

During a non-conservative mass transfer episode, the specific angular momentum of the removed matter is determined by how mass leaves the system. In our `Fiducial` assumption, any non-accreted mass is removed isotropically in the reference frame of the accretor; this mass-loss mode is usually referred to as 'isotropic re-emission' (01). Another common parametrization is the 'Jeans' mode (14), which consists of ejecting the mass isotropically in the reference frame of the donor, similarly to fast winds. The last possibility we take into account is the formation of a circumbinary disc (15), with a radius of $a_{\rm disc} = 2a$ (Artymowicz & Lubow 1994), from which the mass will be ejected. While isotropic re-emission (01) and the 'Jeans' mode (14) tend to effectively widen the orbit, that is not the case if mass is lost from a circumbinary disc (15). The formation rates of Galactic-like DNSs and the log Bayes factor are $\{\mathcal{R}_{14}, \mathcal{R}_{15}\} = \{6.69, 28.05\}$ per Milky Way equivalent galaxy per Myr and $\log\{\mathcal{K}_{14}, \mathcal{K}_{15}\} = \{-3.34, -2.67\}$, respectively. The `Fiducial` model is strongly preferred over the 'Jeans' mode (14) variation; it is also mildly preferred over the circumbinary disc (15) variation. The mass-loss mode also affects the future fate of the formed DNSs. The fraction of all formed DNSs that will merge in a Hubble time is $\{f_{01}, f_{14}, f_{15}\} = \{0.73, 0.21, 0.94\}$ for the 'isotropic re–emission', 'Jeans' and 'circumbinary disc' mode, respectively.

3.2.8 On the CE parameters

We consider several variations to the parameters that govern CE evolution: λ, which determines the envelope binding energy, and α, which determines the amount of orbital energy needed to expel the envelope. In our `Fiducial` model, all of the DNSs experience a CE phase and therefore varying λ and α from the `Fiducial` model choices (i.e. $\lambda_{\rm Nanjing}$ and $\alpha = 1$) will affect the final distributions.

$\lambda_{\rm Nanjing}$ is a function of core mass, total mass, and radius. We use a fixed value $\lambda_{\rm fixed} = 0.1$ (08) for comparison with previous population synthesis studies (e.g. Belczynski et al. 2002). Recently, Kruckow et al. (2016) found for several models at different mass and metallicity that λ depends on the radius in a roughly power-law form $\lambda \propto R^{\beta}$, with $-1 \leq \beta \leq -2/3$. We made a fit to fig. 1 of Kruckow et al. (2016) in the form $\lambda_{\rm Kruckow} = 1600 \times 0.00125^{-\beta} R^{\beta}$, assuming a monotonically decreasing function. For our particular variation, we use an average value where $\beta = -5/6$ (09). The formation rates of DNSs and the log Bayes factors for these variations in λ are $\{\mathcal{R}_{08}, \mathcal{R}_{09}\} = \{16.30, 9.08\}$ per Milky Way equivalent galaxy per Myr and $\log\{\mathcal{K}_{08}, \mathcal{K}_{09}\} = \{-0.07, 0.02\}$, respectively, not favouring nor disfavouring the λ variations with respect to the `Fiducial` model.

Higher values of α lead to wider post-CE orbits than low values of α. Without exploring the full and continuous parameter space, we vary α to extreme values of $\alpha_{\rm min} = 0.1$ (10) and $\alpha_{\rm max} = 10$ (11). Values of $\alpha > 1$ suppose that there are substantial additional energy sources, such as recombination energy and/or nuclear energy (Podsiadlowski et al. 2010; Ivanova et al. 2013) that contribute to the energy budget for CE ejection, in addition to the orbital energy. The extreme value of $\alpha_{\rm max} = 10$ is more for illustration purposes rather than to mimic a particular physical interaction; in this case, $\alpha_{\rm max} = 10$ can only be explained if it comes from nuclear energy. The formation rates of DNSs and the log Bayes factors for variations in α are $\{\mathcal{R}_{10}, \mathcal{R}_{11}\} = \{5.26, 9.54\}$ per Milky Way equivalent galaxy per Myr and $\log\{\mathcal{K}_{10}, \mathcal{K}_{11}\} = \{1.76, -1.97\}$, respectively, neither clearly favouring nor disfavouring the α variations with respect to the `Fiducial` model. The choice of α influences not only the number of created DNSs but also the number of mergers. The fraction of all formed DNSs that will merge in a Hubble time is $\{f_{01}, f_{10}, f_{11}\} = \{0.73, 0.59, 0.36\}$.

Additionally, we also consider the 'pessimistic' CE assumption (19). This assumption yields a DNS population that is a subset of the population under the `Fiducial` model, with binaries that enter the CE while the donor is classified as a HG star removed, as these are assumed to always lead to merger. The 'pessimistic' CE assumption (19) is therefore expected to decrease DNS formation rates. The formation rates of DNSs and the log Bayes factors for these variations are $\{\mathcal{R}_{01}, \mathcal{R}_{19}\} = \{24.04, 14.29\}$ per Milky Way equivalent galaxy per Myr and $\log\{\mathcal{K}_{01}, \mathcal{K}_{19}\} = \{0, -0.16\}$, respectively. The likelihood of the 'pessimistic' model (19) is similar to the one from the `Fiducial` model, which means the *P*–*e* distribution alone is insufficient to pick between these models. Additional constraints, such as merger rates, would be needed to determine the preferred model.

3.2.9 On the effect of thermal eccentricity

The only initial distribution we varied in this study was eccentricity. In order to simulate a population with non-circular binaries at ZAMS we use the thermal eccentricity distribution (16), which has the form of $f_{\rm e}(e) = 2e$ (Heggie 1975). In this variation, the first episode of mass transfer begins once the primary expands to fill its Roche lobe at periastron. This changes the range of initial periods leading to interaction (de Mink & Belczynski 2015).

The formation rate and log Bayes factor of model (16) are $\mathcal{R} = 10.22$ per Milky Way equivalent galaxy per Myr and $\log \mathcal{K} = -0.07$, respectively. While formation rates drop by a factor of approximately 3, the *P*–*e* distribution of forming DNSs is not significantly affected. The drop in the formation rate is due to enhanced rates of interactions of MS stars that only need to fill their Roche lobe at periastron; if that mass transfer episode is unstable, the two MS stars merge.

3.3 On mass ratio distributions

Fig. 3 shows the impact of the choice of the SN remnant mass model on the DNS mass ratio distributions. The `Fiducial` model shows two distinct peaks in the mass ratio distribution around $q_{\rm DCO} = 0.87$ and $q_{\rm DCO} = 1$. The two peaks can be explained given the evolution of *Channel I* and *Channel II*, respectively. For the full discussion on the characteristics of the mass ratio for the `Fiducial` model (see Section 3.1.2).

In the 'delayed' prescription (03), most of the USSNe change mass from 1.1 to 1.28 $M_{\odot}$, with respect to the 'rapid' mechanism; therefore, the mass ratio of systems where the primary collapsed in an ECSN and the secondary in an USSN approaches 1, yielding an even more dominant peak at $q_{\rm DCO} = 1$ in the overall mass ratio distribution. *Channel II* leads to the second peak, with mass ratio $q_{\rm DCO} = 1$, as in the `Fiducial` model. This results in a cumulative

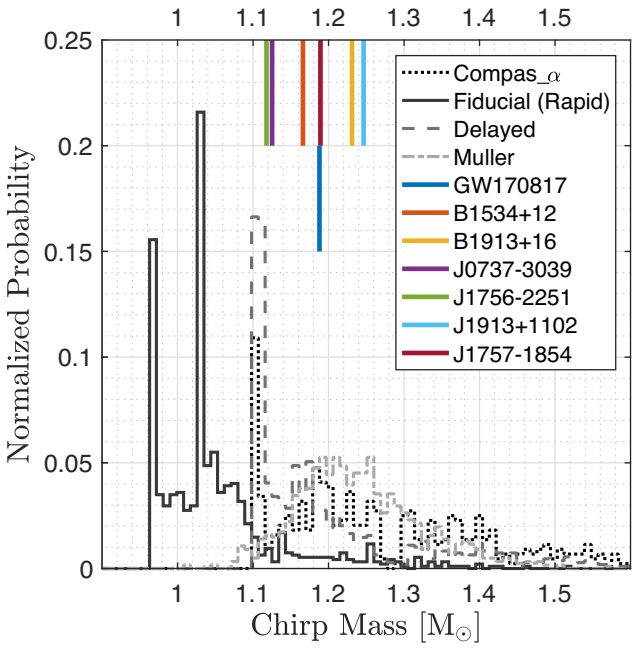

Figure 10. Chirp mass distribution of DNSs with a delay time smaller than a Hubble time: (00) COMPAS_α (black dotted), (01) `Fiducial` Fryer Rapid (dark grey solid), (03) Fryer Delayed (grey dashed), and (04) Müller (light grey dot–dashed). Galactic DNSs with an estimated delay time smaller than a Hubble time are indicated at the top. GW170817, the only GW signal detected from DNSs to date, is shown as a vertically offset thick green line, with a similar chirp mass (1.188 $M_\odot$) as J1757–1854 in purple. All systems have precise mass measurements with error bars within the thickness of the line.

distribution function for the 'delayed' mechanism (03) with a mass ratio between $0.52 \leq q_{\rm DCO} \leq 1$, where 80 per cent of the systems have $q_{\rm DCO} > 0.80$, 55 per cent have $q_{\rm DCO} > 0.90$, and 40 per cent have $q_{\rm DCO} > 0.95$.

The remnant masses in the Müller prescription (04), as shown in Figs 7 and B1, have a wider spread and vary more at the low-mass end. In this model, there is no significant pile-up. There is more scatter, with 70 per cent of the systems having $q_{\rm DCO} > 0.8$, 40 per cent having $q_{\rm DCO} > 0.9$, and 20 per cent having $q_{\rm DCO} > 0.95$.

3.4 On the chirp mass distribution

Fig. 10 shows the chirp mass distributions of DNSs that will merge within a Hubble time. We compare the prediction of our `Fiducial` model (01) that uses the 'rapid' explosion mechanism, to the model which uses the 'delayed' (03) explosion mechanism and to that which uses the 'Müller' (04) prescription.

Additionally, we also show the COMPAS_α (00) chirp mass distribution that uses the 'delayed' mechanism. As expected, the chirp mass distributions show similarities with the mass ratio distributions, reproducing the same sharp features (peaks) explained in Section 3.3. In Fig. 10, we added all the confirmed DNSs with an estimated delay time smaller than the Hubble time, as well as GW170817.

We find that the 'rapid' (01) mechanism predicts that most of the DNSs will have chirp mass lower than J1756–2251, which has the lowest chirp mass among confirmed DNSs with good mass constraints. In fact, the 'rapid' SN mechanism (01) allows for low-mass NSs, which would be difficult to differentiate from NS–white dwarf binaries; there are several non-confirmed DNSs or poorly constrained DNS masses in the region favoured by the 'rapid' mechanism (01) (Özel et al. 2010; Özel & Freire 2016). On the other hand, the seven existing well-constrained mass measurements in this study are inconsistent with the predictions of the `Fiducial` model (01) at a $>4\sigma$ level. None of these seven measurements fall below a chirp mass of 1.1 $M_\odot$, while 83 per cent of DNSs in the `Fiducial` model have lower chirp masses. This suggests that the 'rapid' mechanism underpredicts the amount of collapsed mass for the lowest-mass NSs for both ECSNe and USSNe.

All other SN prescriptions considered here yield DNS chirp mass distributions starting above 1.1 $M_\odot$. Unsurprisingly, the 'delayed' mechanism (03) has a very similar distribution to COMPAS_α that uses the same explosion mechanism. They both predict systems matching all chirp masses (see Fig. 10), with a peak close to the lowest observed DNS chirp masses, J1756–2251 and J0737–3039. The 'Müller' prescription (04) yields a similarly broad chirp mass distribution above 1.1 $M_\odot$. The 'delayed' (03) and 'Müller' (04) SN fallback prescriptions cannot be distinguished based on existing mass measurements. However, the separation of $\approx$0.4 between the predicted chirp mass cumulative distribution functions for these two models suggests that $\sim$ 10 additional chirp mass measurements (whether from radio pulsars or merging DNSs) would be sufficient to tell these models apart.

3.5 On kicks

When binaries survive an SN explosion, they may get significant centre-of-mass kicks from both natal NS kicks and Blaauw recoil (Blaauw 1961) from mass-loss. The resulting DNS population should therefore be more broadly spatially distributed in the Galaxy than the regions of massive star formation. We follow a population of `Fiducial` model DNSs with the predicted total kick distribution in a Galactic potential starting from birth in the thin disc. While we find that, as expected, kicks broaden the distribution of Galactocentric distances (see Fig. C1 in Appendix C, where the details of this analysis are presented), the deep Galactic potential well means that this broadening is relatively small and challenging to test for. In practice, the spreading of DNSs away from the thin disc may be even smaller than estimated here, because our simplified case BB mass-loss models imply fairly high remaining core masses, between $1.6 \leq m_{\rm CO}/M_\odot \leq 4.6$, while detailed calculations of ultra-stripping suggest lower remnant core masses $1.45 \leq m/M_\odot \leq 3.15$ (Tauris et al. 2015). Reducing COMPAS core masses in line with Tauris et al. (2015) would both reduce Blaauw kicks and DNS eccentricities. On the other hand, three quarters of short GRBs are found outside the effective radius of the host galaxy (Fong & Berger 2013), providing a strong constraint on the binary natal kick distribution; Fong & Berger (2013) estimate total kicks of $\approx$20–140 km s^{-1}.

3.6 On rates

3.6.1 DNS merger rates

DNS formation and merger rates are constrained by the observed sample of Galactic binary pulsars (e.g. Kim, Kalogera & Lorimer 2003; O'Shaughnessy & Kim 2010), by observations of short GRBs (Fong & Berger 2013), and will ultimately be measured with gravitational-wave observations (see Mandel & O'Shaughnessy 2010 for a review). Rates inferred from Galactic binary pulsars are dominated by a few systems and are sensitive to the imperfectly known pulsar radio luminosity distribution (Kalogera et al. 2004).

Short GRBs extend the observations beyond the Milky Way to cosmological distances, but inference from these is complicated by the difficulty of measuring jet opening angles and uncertain selection effects, and relies on the additional assumption of a one-to-one correspondence between short GRBs and DNS mergers (Berger 2014). Abadie et al. (2010) combined the existing observational constraints to suggest that the DNS merger rate lies between 1 and 1000 Myr^{-1} in a Milky Way equivalent galaxy (approximately 10–10 000 $\mathrm{Gpc}^{-3}\,\mathrm{yr}^{-1}$), with a likely value toward the middle of this range. All of the models presented here fall within this range, although we focus on the Milky Way DNS population rather than the merger rate, and hence did not consider the convolution of the DNS formation rate and delay time distribution over cosmic history.

Other recent population synthesis studies give estimates that, like ours, fall in the two lower decades of this range. Chruslinska et al. (2018) use StarTrack to predict a local merger rate density of 48 $\mathrm{Gpc}^{-3}\,\mathrm{yr}^{-1}$ for their standard assumptions and 600^{+600}_{-300} $\mathrm{Gpc}^{-3}\,\mathrm{yr}^{-1}$ for a very optimistic set of assumptions. Belczynski et al. (2018) also use StarTrack to argue that even these rates are two orders of magnitude larger than the contribution from globular or nuclear clusters. Kruckow et al. (2018) use ComBinE to predict an upper limit of local merger rate of 400 $\mathrm{Gpc}^{-3}\,\mathrm{yr}^{-1}$.

Meanwhile, Abbott et al. (2017c) estimate a DNS merger rate of 1540^{+3200}_{-1220} $\mathrm{Gpc}^{-3}\,\mathrm{yr}^{-1}$ based on GW170817 alone. However, given the significant Poisson uncertainty and sensitivity to rate priors from a single observation,[5] the addition of this one (albeit, very special) event to the population of merging Galactic DNSs and short GRBs does not significantly shift the observational constraints on the DNS merger rate. In fact, given the similarity of the predicted DNS formation rates among most models presented here, observational constraints on the rate alone will not be sufficient to distinguish between these models in the near future.

3.6.2 *SN rates*

We estimate the SN rates for our `Fiducial` model (01). Given the ambiguity in SN classification, we make simplifying assumptions to convert our models into observational predictions. We consider all progenitors with a hydrogen envelope to lead to hydrogen-rich SNe (type II excluding type IIb) and the rest are considered stripped SNe (either hydrogen absent type Ib or Ic or hydrogen-poor type IIb). Our total rate of SNe leading to NS formation is 0.0080 per $\mathrm{M}_\odot$, which includes both ECSNe and USSNe. Among these, 75.6 per cent are hydrogen rich and the remaining 24.4 per cent are classified as stripped SNe, including all USSNe. We predict that USSNe that follow after case BB mass transfer on to an NS companion should make up 1.2 per cent of all stripped SNe and 0.3 per cent of all SNe leading to NS formation.

Our total SN rate prediction is consistent with Zapartas et al. (2017), a population synthesis study that reports CCSN rates in binaries between 0.0035–0.0253 per $\mathrm{M}_\odot$, depending on the assumed IMF. Our estimates for the fraction of stripped SNe compare well with observational results. Eldridge et al. (2013) find that the fractions of hydrogen rich and stripped SNe leading to NS formation are 61.9 per cent and 38.1 per cent, respectively; that study was made with SNe discovered between 1998 and 2012 in galaxies with recessional velocities less than 2000 $\mathrm{km\,s}^{-1}$. More recently, Shivvers et al. (2017) report that 69.6 per cent of CCSNe are hydrogen rich (according to the definition above), while the remaining 30.4 per cent come from stars with stripped envelopes.

[5]For example, shifting from a flat-in-rate prior to a $p(R) \propto 1/\sqrt{R}$ Jeffreys prior (Jeffreys 1946) would reduce the peak of the posterior by a factor of 2 following one detection. Furthermore, the posterior peak is a factor of 1.67 lower than the posterior median quoted by Abbott et al. (2017c).

4 DISCUSSION AND CONCLUSIONS

We used the COMPAS rapid population synthesis code to follow the evolution of massive stellar binaries and thus generate a population of DCOs. We quantitatively validated our models by comparing the predicted P–e distribution of DNSs against the observed Galactic DNS distribution, and qualitatively compared the predicted rate and mass distribution of Galactic DNSs to observations. We considered variations relative to the `Fiducial` model in order to investigate the impact of uncertain evolutionary physics. We find the following:

(i) Case BB mass transfer during DNS formation must be predominantly stable. We considered the possibility that HeHG of the secondary leads to dynamically unstable mass transfer and a second CE phase (Dewi & Pols 2003) in Variation (02). In fact, this was our initial default model, consistent with COMPAS_α (00) in this assumption. However, the lack of DNSs with few-hour orbital periods (such as J0737–3039) in this variation (see Fig. 8), as well as our Bayesian analysis indicates that most case BB mass transfer episodes must be stable. This finding is consistent with the detailed models of Tauris et al. (2015). However, some case BB dynamically unstable systems could exist without being detectable in the observed DNS population: the very short orbital periods of DNSs that were hardened by two CE phases would lead them to merge in less than a few hundred thousand years. While our study assumes constant star formation within the history of the Galaxy, the short orbital period DNSs would be disfavoured in Galactic star formation history models without recent periods of starbursts.

(ii) A bimodal SN natal kick distribution is preferred over a single mode one. We find that a bimodal natal kick distribution (with non-zero components) with lower natal kicks for ECSNe and USSNe and higher natal kicks for standard CCSNe is preferred [see variations (05), (06), (07)]. If ECSNe and/or USSNe are given the high natal kicks consistent with the observed velocities of isolated pulsars (Hansen & Phinney 1997; Hobbs et al. 2005), wider binaries are overwhelmingly disrupted by SNe, and observed wide DNSs cannot be reproduced in the models. A bimodal SN natal kick distribution is consistent with the findings of other population synthesis studies [see Belczynski et al. (2002) and Pfahl et al. (2002b) as well as with comparison to observations from Schwab et al. (2010), Beniamini & Piran (2016), and Verbunt et al. (2017)], although O'Shaughnessy et al. (2008) did not find evidence for multiple natal kick distributions.

The aforementioned findings in our paper, stability during case BB mass transfer and a bimodal natal kick distribution are broadly in agreement with those in Andrews et al. (2015), which used a smaller sample of eight Galactic DNSs instead of the current 14 confirmed systems and carried out population synthesis by mainly varying CE parameters and natal kick magnitudes. Andrews et al. (2015) find that it is likely that short-period low-eccentricity systems went through an evolutionary channel that includes stable case BB mass transfer. Their study also points out that the cores of ECSN progenitors should have relatively low mass, which can be related to lower natal kick magnitude.

(iii) Predicted DNS formation rates across variations are consistent with observations. The formation rate of DNSs in the `Fiducial` model is 24 Myr^{-1} in the Milky Way. The Milky Way DNS

formation rate for all considered variations is 5–31 Myr^{-1}. All rates are consistent with observations (Abadie et al. 2010), including the inferred rate from the GW170817 gravitational-wave detection (Abbott et al. 2017c), and cannot be used to differentiate between the models at this point.

We also considered multiple SN explosion mechanisms, including varying the fallback mass [Fryer 'rapid' (01) and Fryer 'delayed' (03) variations] and a coupled mass–kick model calibrated to numerical simulations ['Müller' (04) prescription].

Low-mass iron-core CCSNe may have reduced natal kicks, but are given standard CCSN natal kicks in the Fryer models, including the `Fiducial` model. The mass distribution of observed systems is not consistent with the very low masses predicted by the Fryer 'rapid' fallback prescription used in the `Fiducial` model (01). Furthermore, observations do not show a peak in the mass distribution around 1.26 $M_\odot$, where ECSNe should fall in our models. The remnant mass of an ECSN depends on the NS's equation of state and indicates either that ECSNe are less common in binaries than we expected or that the ECSN models should be revisited, as similarly noticed by Kruckow et al. (2018). With only ∼10 additional DNS mass measurements, it will be possible to further constrain the SN fallback mechanisms, distinguishing between the 'Müller' (04) and Fryer 'delayed' (03) variants, both of which are consistent with existing observations.

Further input on natal kick velocity distributions should come from a better comparison with observed isolated pulsar natal kicks. At the moment, the observed isolated pulsar distribution is used to calibrate the CCSN natal kicks in binaries. However, the sample of observed isolated pulsars is contaminated by pulsars from disrupted binaries. Therefore, the approach we used here, which is also used by most population-synthesis codes, is not self-consistent: the observed single-pulsar velocity distribution should be checked for consistency against a model that includes contributions from both single and binary massive stars. In particular, observations should be tested for evidence of the predicted low natal kicks associated with ECSNe, which may preferentially occur in binaries (Podsiadlowski et al. 2004) that may subsequently be disrupted.

We assumed a solar metallicity $Z_\odot = 0.0142$ for massive stars in the Galaxy. In reality, the Galaxy has a distribution of metallicities at the present day, as well as a history of metallicity evolution over time, since present-day DNS systems and particularly DNS mergers may have formed at earlier times or in lower-metallicity regions [see Lamberts et al. (2018) for a discussion of Galactic binary BH formation]. While Fig. 9 confirms that, for a suitable choice of metallicity and initial conditions, the `Fiducial` model can produce compact binary mergers with masses matching all of the existing gravitational-wave observations; it also demonstrates that metallicity does impact the rate and properties of merging DNSs. Therefore, the metallicity-specific star formation history of the Milky Way could affect the details of the modelled DNS population.

We do not account for selection effects in the observed Galactic DNS population in this study [see Tauris et al. (2017) for a detailed discussion]. Binaries with very short orbital periods may be selected against because of the orbital acceleration of the pulsar, which changes the apparent spin period; they will also have short merger times, and their location within the Galaxy will be sensitive to the details of recent star formation history. Meanwhile, binaries with extremely long orbital periods may also be challenging to detect, since they are less likely to be recycled during binary evolution, and detectable radio emission from non-recycled pulsars is expected to last for $\lesssim$50 Myr (Lorimer & Kramer 2004).

The DNS formation models presented here can also be tested against observable populations of massive stars during intermediate phases before DNS formation. Neutron star Be/X-ray binaries (e.g. Knigge, Coe & Podsiadlowski 2011) offer a particularly promising test case; for example, the observed correlation between the orbital period and the NS spin, with the latter appearing to be bimodal, could indicate distinct SN classes in their evolutionary history (Knigge et al. 2011). Spin distribution predictions could also be compared to observed pulsar spin periods in both isolated pulsars (e.g. Kiel et al. 2008) and in DNS systems (e.g. Dewi, Podsiadlowski & Pols 2005; Osłowski et al. 2011; Tauris et al. 2017). However, determining the NS spin-up or spin-down through binary interactions and pulsar evolution requires additional modelling assumptions, and hence spin models were not included in the present study. Meanwhile, more detailed studies of natal kicks in the Galactic potential could lead to additional constraints on natal kick distributions. Moreover, gravitational-wave detections will produce an ever larger catalogue of accurate mass measurements, at least for the chirp mass parameter. Together, these growing observational data sets will enable increasingly accurate tests of the massive stellar binary evolution models described here.

ACKNOWLEDGEMENTS

AVG acknowledges support from Consejo Nacional de Ciencia y Tecnologia (CONACYT) and thanks the PHAROS European Cooperation in Science and Technology (COST) Action (CA16214) for partial support. IM acknowledges partial support from the Science and Technology Facilities Council (STFC). KB acknowledges support from the Polish National Science Center (NCN) grants Sonata Bis 2 (DEC-2012/07/E/ST9/01360) and OPUS (2015/19/B/ST9/01099). SJ is partially supported by the Strategic Priority Research Program of the Chinese Academy of Sciences 'Multi-waveband Gravitational Wave Universe' (grant no. XDB23040000), and is also grateful to the Chinese Academy of Sciences (President's International Fellowship Initiative grant no. 2011Y2JB07) and the National Natural Science Foundation of China (grant no. 11633005). SdM acknowledges the European Union's Horizon 2020 research and innovation programme for funding from the European Research Council (ERC), grant agreement no. GS100010663. SdM and IM acknowledge the hospitality of the Kavli Institute for Theoretical physics, Santa Barbara, CA. Their stay was supported by the National Science Foundation under grant no. NSF PHY11-25915. BM was supported by the Australian Research Council (ARC) through ARC Future Fellowship FT160100035. SS was supported by the Australian Research Council Centre of Excellence for Gravitational Wave Discovery (OzGrav), CE170100004.

We thank the Niels Bohr Institute for its hospitality while part of this work was completed, and acknowledge the Kavli Foundation and the Danish National Research Foundation (DNRF) for supporting the 2017 Kavli Summer Program. We also thank Jeff Andrews, Christopher Berry, Ross Church, David Stops, Jason Hessels, Serena Vinciguerra, and Manos Zapartas for discussions, suggestions, and assistance during the writing of this manuscript.

REFERENCES

Abadie J. et al., 2010, Class. Quantum Gravity, 27, 173001
Abbott B. P. et al., 2016a, Phys. Rev. X, 6, 041015

Abbott B. P. et al., 2016b, Phys. Rev. Lett., 116, 061102
Abbott B. P. et al., 2016c, Phys. Rev. Lett., 116, 241103
Abbott B. P. et al., 2017a, Phys. Rev. Lett., 118, 221101
Abbott B. P. et al., 2017b, Phys. Rev. Lett., 119, 141101
Abbott B. P. et al., 2017c, Phys. Rev. Lett., 119, 161101
Anderson S. B., Gorham P. W., Kulkarni S. R., Prince T. A., Wolszczan A., 1990, Nature, 346, 42
Andrews J. J., Farr W. M., Kalogera V., Willems B., 2015, ApJ, 801, 32
Artymowicz P., Lubow S. H., 1994, ApJ, 421, 651
Arzoumanian Z., Chernoff D. F., Cordes J. M., 2002, ApJ, 568, 289
Asplund M., Grevesse N., Sauval A. J., Scott P., 2009, ARA&A, 47, 481
Barrett J. W., Gaebel S. M., Neijssel C. J., Vigna-Gómez A., Stevenson S., Berry C. P. L., Farr W. M., Mandel I., 2018, MNRAS, 477, 4685
Belczyński K., Bulik T., 1999, A&A, 346, 91
Belczynski K., Kalogera V., Bulik T., 2002, ApJ, 572, 407
Belczynski K., Kalogera V., Rasio F. A., Taam R. E., Zezas A., Bulik T., Maccarone T. J., Ivanova N., 2008, ApJS, 174, 223
Belczynski K., Holz D. E., Bulik T., O'Shaughnessy R., 2016, Nature, 534, 512
Belczynski K. et al., 2018, A&A, 615, A19
Belczyński K., Kalogera V., 2001, ApJ, 550, L183
Beniamini P., Piran T., 2016, MNRAS, 456, 4089
Berger E., 2014, ARA&A, 52, 43
Bhattacharya D., van den Heuvel E. P. J., 1991, Phys. Rep., 203, 1
Blaauw A., 1961, Bull. Astron. Inst. Netherlands, 15, 265
Brandt N., Podsiadlowski P., 1995, MNRAS, 274, 461
Bray J. C., Eldridge J. J., 2016, MNRAS, 461, 3747
Brisken W. F., Benson J. M., Goss W. M., Thorsett S. E., 2002, ApJ, 571, 906
Brown G. E., 1995, ApJ, 440, 270
Cameron A. D. et al., 2018, MNRAS, 475, L57
Champion D. J., Lorimer D. R., McLaughlin M. A., Cordes J. M., Arzoumanian Z., Weisberg J. M., Taylor J. H., 2004, MNRAS, 350, L61
Chomiuk L., Povich M. S., 2011, AJ, 142, 197
Chruslinska M., Belczynski K., Klencki J., Benacquista M., 2018, MNRAS, 474, 2937
Church R. P., Levan A. J., Davies M. B., Tanvir N., 2011, MNRAS, 413, 2004
Claeys J. S. W., Pols O. R., Izzard R. G., Vink J., Verbunt F. W. M., 2014, A&A, 563, A83
Corongiu A., Kramer M., Stappers B. W., Lyne A. G., Jessner A., Possenti A., D'Amico N., Löhmer O., 2007, A&A, 462, 703
de Kool M., 1990, ApJ, 358, 189
de Mink S. E., Belczynski K., 2015, ApJ, 814, 58
de Mink S. E., Pols O. R., Hilditch R. W., 2007, A&A, 467, 1181
del Peloso E. F., da Silva L., Porto de Mello G. F., Arany-Prado L. I., 2005, A&A, 440, 1153
Dewi J. D. M., Pols O. R., 2003, MNRAS, 344, 629
Dewi J. D. M., Podsiadlowski P., Pols O. R., 2005, MNRAS, 363, L71
Dewi J. D. M., Podsiadlowski P., Sena A., 2006, MNRAS, 368, 1742
Dominik M., Belczynski K., Fryer C., Holz D. E., Berti E., Bulik T., Mandel I., O'Shaughnessy R., 2012, ApJ, 759, 52
Eggleton P. P., 1983, ApJ, 268, 368
Eldridge J. J., Fraser M., Smartt S. J., Maund J. R., Crockett R. M., 2013, MNRAS, 436, 774
Farr W. M., Sravan N., Cantrell A., Kreidberg L., Bailyn C. D., Mandel I., Kalogera V., 2011, ApJ, 741, 103
Faulkner A. J. et al., 2005, ApJ, 618, L119
Fong W., Berger E., 2013, ApJ, 776, 18
Fonseca E., Stairs I. H., Thorsett S. E., 2014, ApJ, 787, 82
Fryer C. L., Belczynski K., Wiktorowicz G., Dominik M., Kalogera V., Holz D. E., 2012, ApJ, 749, 91
Ge H., Webbink R. F., Chen X., Han Z., 2015, ApJ, 812, 40
Götberg Y., de Mink S. E., Groh J. H., 2017, A&A, 608, A11
Grindlay J., Portegies Zwart S., McMillan S., 2006, Nature Phys., 2, 116
Hansen B. M. S., Phinney E. S., 1997, MNRAS, 291, 569
Heggie D. C., 1975, MNRAS, 173, 729
Hobbs G., Lorimer D. R., Lyne A. G., Kramer M., 2005, MNRAS, 360, 974
Hulse R. A., Taylor J. H., 1975, ApJ, 195, L51
Hurley J. R., Pols O. R., Tout C. A., 2000, MNRAS, 315, 543
Hurley J. R., Tout C. A., Pols O. R., 2002, MNRAS, 329, 897
Hwang J., Lombardi J. C., Jr, Rasio F. A., Kalogera V., 2015, ApJ, 806, 135
Irrgang A., Wilcox B., Tucker E., Schiefelbein L., 2013, A&A, 549, A137
Ivanova N., Heinke C. O., Rasio F. A., Belczynski K., Fregeau J. M., 2008, MNRAS, 386, 553
Ivanova N. et al., 2013, A&AR, 21, 59
Izzard R. G., Tout C. A., Karakas A. I., Pols O. R., 2004, MNRAS, 350, 407
Izzard R. G., Dray L. M., Karakas A. I., Lugaro M., Tout C. A., 2006, A&A, 460, 565
Izzard R. G., Glebbeek E., Stancliffe R. J., Pols O. R., 2009, A&A, 508, 1359
Janka H.-T., 2017, ApJ, 837, 84
Janssen G. H., Stappers B. W., Kramer M., Nice D. J., Jessner A., Cognard I., Purver M. B., 2008, A&A, 490, 753
Jaynes E., Jaynes E., Bretthorst G., Press C. U., 2003, Probability Theory: The Logic of Science. Cambridge Univ. Press, Cambridge
Jeffreys H., 1946, Proc. R. Soc. London Ser. A, 186, 453
Kalogera V. et al., 2004, ApJ, 601, L179
Katz J. I., 1975, Nature, 253, 698
Keith M. J., Kramer M., Lyne A. G., Eatough R. P., Stairs I. H., Possenti A., Camilo F., Manchester R. N., 2009, MNRAS, 393, 623
Kiel P., Hurley J., Bailes M., Murray J., 2008, MNRAS, 388, 393
Kim C., Kalogera V., Lorimer D. R., 2003, ApJ, 584, 985
Kippenhahn R., Weigert A., 1967, Z. Astrophys., 65, 251
Knigge C., Coe M. J., Podsiadlowski P., 2011, Nature, 479, 372
Kramer M. et al., 2006, Science, 314, 97
Kreidberg L., Bailyn C. D., Farr W. M., Kalogera V., 2012, ApJ, 757, 36
Kroupa P., 2001, MNRAS, 322, 231
Kruckow M. U., Tauris T. M., Langer N., Szécsi D., Marchant P., Podsiadlowski P., 2016, A&A, 596, A58
Kruckow M. U., Tauris T. M., Langer N., Kramer M., Izzard R. G., 2018, MNRAS, 481, 1908
Lamberts A. et al., 2018, MNRAS, 480, 2704
Lazarus P. et al., 2016, ApJ, 831, 150
Lentz E. J. et al., 2015, ApJ, 807, L31
Lorimer D. R., Kramer M., 2004, Handbook of Pulsar Astronomy. Cambridge Univ. Press, Cambridge
Lynch R. S., Freire P. C. C., Ransom S. M., Jacoby B. A., 2012, ApJ, 745, 109
MacLeod M., Ramirez-Ruiz E., 2015, ApJ, 798, L19
Mandel I., O'Shaughnessy R., 2010, Class. Quantum Gravity, 27, 114007
Marek A., Janka H., 2009, ApJ, 694, 664
Martinez J. G. et al., 2015, ApJ, 812, 143
Martinez J. G. et al., 2017, ApJ, 851, L29
Melson T., Janka H.-T., Marek A., 2015a, ApJ, 801, L24
Melson T., Janka H.-T., Bollig R., Hanke F., Marek A., Müller B., 2015b, ApJ, 808, L42
Müller B., Heger A., Liptai D., Cameron J. B., 2016, MNRAS, 460, 742
Müller B., Melson T., Heger A., Janka H.-T., 2017, MNRAS, 472, 491
Nomoto K., 1984, ApJ, 277, 791
Nomoto K., 1987, ApJ, 322, 206
Nordhaus J., Brandt T. D., Burrows A., Livne E., Ott C. D., 2010, Phys. Rev. D, 82, 103016
O'Shaughnessy R., Kim C., 2010, ApJ, 715, 230
O'Shaughnessy R., Kim C., Fragos T., Kalogera V., Belczynski K., 2005, ApJ, 633, 1076
O'Shaughnessy R., Kim C., Kalogera V., Belczynski K., 2008, ApJ, 672, 479
Osłowski S., Bulik T., Gondek-Rosińska D., Belczyński K., 2011, MNRAS, 413, 461
Öpik E., 1924, Publ. Tartu Astrofizica Obs., 25
Özel F., Freire P., 2016, ARA&A, 54, 401
Özel F., Psaltis D., Narayan R., McClintock J. E., 2010, ApJ, 725, 1918
Paczynski B., 1976, in Eggleton P., Mitton S., Whelan J., eds, Proc. IAU Symp. 73, Structure and Evolution of Close Binary Systems. Reidel, Dordrecht, p. 75

Pavlovskii K., Ivanova N., Belczynski K., Van K. X., 2017, MNRAS, 465, 2092
Peters P. C., 1964, Phys. Rev., 136, B1224
Pfahl E., Rappaport S., Podsiadlowski P., 2002a, ApJ, 571, L37
Pfahl E., Rappaport S., Podsiadlowski P., Spruit H., 2002b, ApJ, 574, 364
Phinney E. S., Sigurdsson S., 1991, Nature, 349, 220
Planck Collaboration XIII, 2016, A&A, 594, A13
Podsiadlowski P., Langer N., Poelarends A. J. T., Rappaport S., Heger A., Pfahl E., 2004, ApJ, 612, 1044
Podsiadlowski P., Ivanova N., Justham S., Rappaport S., 2010, MNRAS, 406, 840
Poelarends A. J. T., Herwig F., Langer N., Heger A., 2008, ApJ, 675, 614
Poelarends A. J. T., Wurtz S., Tarka J., Cole Adams L., Hills S. T., 2017, ApJ, 850, 197
Pols O. R., 1994, A&A, 290, 119
Pols O. R., Schröder K.-P., Hurley J. R., Tout C. A., Eggleton P. P., 1998, MNRAS, 298, 525
Portegies Zwart S. F., Verbunt F., 1996, A&A, 309, 179
Portegies Zwart S. F., Yungelson L. R., 1998, A&A, 332, 173
Sana H. et al., 2012, Science, 337, 444
Scheck L., Plewa T., Janka H.-T., Kifonidis K., Müller E., 2004, Phys. Rev. Lett., 92, 011103
Scheck L., Kifonidis K., Janka H.-T., Müller E., 2006, A&A, 457, 963
Schwab J., Podsiadlowski P., Rappaport S., 2010, ApJ, 719, 722
Shivvers I. et al., 2017, PASP, 129, 054201
Silverman B. W., 1986, Density Estimation for Statistics and Data Analysis. CRC Press
Sivia D., 1996, Data Analysis: A Bayesian Tutorial. Oxford University Press, Oxford
Smartt S. J., 2015, PASA, 32, 16
Soberman G. E., Phinney E. S., van den Heuvel E. P. J., 1997, A&A, 327, 620
Stevenson S., Vigna-Gómez A., Mandel I., Barrett J. W., Neijssel C. J., Perkins D., de Mink S. E., 2017, Nature Commun., 8, 14906
Stovall K. et al., 2018, ApJ, 854, L22
Summa A., Hanke F., Janka H.-T., Melson T., Marek A., Müller . B., 2016, ApJ, 825, 6
Swiggum J. K. et al., 2015, ApJ, 805, 156
Tauris T. M., van den Heuvel E. P. J., 2006, Formation and Evolution of Compact Stellar X-ray Sources. Cambridge Univ. Press, Cambridge, p. 623
Tauris T. M., Langer N., Moriya T. J., Podsiadlowski P., Yoon S.-C., Blinnikov S. I., 2013, ApJ, 778, L23
Tauris T. M., Langer N., Podsiadlowski P., 2015, MNRAS, 451, 2123
Tauris T. M. et al., 2017, ApJ, 846, 170
The LIGO Scientific Collaboration et al., 2017, ApJ, 851, L35
Timmes F. X., Woosley S. E., Weaver T. A., 1996, ApJ, 457, 834
Toonen S., Nelemans G., Portegies Zwart S., 2012, A&A, 546, A70
Tutukov A. V., Yungel'son L. R., 1993, AZh, 70, 812
Verbunt F., Cator E., 2017, J. Astrophys. Astron., 38, 40
Verbunt F., Igoshev A., Cator E., 2017, A&A, 608, A57
Voss R., Tauris T. M., 2003, MNRAS, 342, 1169
Wanajo S., Janka H.-T., Müller B., 2011, ApJ, 726, L15
Webbink R. F., 1984, ApJ, 277, 355
Wongwathanarat A., Janka H.-T., Müller E., 2013, A&A, 552, A126
Woosley S. E., Heger A., 2015, ApJ, 810, 34
Wyrzykowski Ł. et al., 2016, MNRAS, 458, 3012
Xu X.-J., Li X.-D., 2010, ApJ, 716, 114
Zapartas E. et al., 2017, A&A, 601, A29

APPENDIX A: LIKELIHOOD CALCULATION

Our methodology follows Andrews et al. (2015). We can write the base e log-likelihood $\log \mathcal{L}$ as

$$\log \mathcal{L} = \sum_{b=1}^{N_{\rm obs}} \log\ p(\log P_b, e_b|M), \tag{A1}$$

where e_b and $\log P_b$ are the eccentricity and log of the orbital period in days for the bth observed DNS, respectively; $N_{\rm obs} = 14$ observations were used here (see Table 1 and associated discussion). The term $p(\log P_b, e_b|M)$ describes the likelihood of observing the b-th DNS given a model M, where our models are described in Table 2 and shown in Fig. A1. We therefore need a way of calculating the 2D probability density given the discrete simulated DNS binaries we have for each model.

We evolve the eccentricity and period of each simulated DNS, as it emits gravitational radiation according to Peters (1964). We stop the inspiral evolution when the system either merges or reaches 10 Gyr (a proxy for the age of the Galactic thin disc, see del Peloso et al. 2005). We place systems into linearly spaced bins in eccentricity, with the lowest bin spanning $e \in [0, 10^{-4}]$, and determine the log period $\log P_k$ when the system enters each bin with eccentricity e_k and the time the system spends in that bin Δt_k, which is subject to

$$\sum_k \Delta t_k = t_{\rm delay}. \tag{A2}$$

We weigh the contribution of each binary at each point in its evolutionary history to the probability density map by Δt_k, since a system is more likely to be observed in the part of the orbit where it spends more of its time. Since tight, highly eccentric binaries evolve the fastest due to gravitational radiation, this has the effect of down weighting those binaries in our analysis (see Fig. 2).

We construct the probability density map from a discrete sample of simulated binaries by means of a weighted kernel density estimator.[6] We model the 2D probability density as a sum of weighted Gaussians

$$p(\log P, e|M) = \sum_{j=1}^{n_{\rm binaries}} \sum_{k=1}^{n_{\text{time-steps},\,j}} \frac{\Delta t_k}{T} N(\boldsymbol{\mu}_k, \boldsymbol{\Sigma}_k), \tag{A3}$$

where

$$T = \sum_{j=1}^{n_{\rm binaries}} \sum_{k=1}^{n_{\text{time-steps},\,j}} \Delta t_k = \sum_{j=1}^{n_{\rm binaries}} t_{\text{delay},\,j}; \tag{A4}$$

$N(\boldsymbol{\mu}, \boldsymbol{\Sigma})$ is the 2D normal distribution with mean

$$\boldsymbol{\mu}_k = (\log\ P_k, e_k), \tag{A5}$$

and the covariance $\boldsymbol{\Sigma}_k$ is chosen to be the same for all samples

$$\boldsymbol{\Sigma}_k = \begin{bmatrix} b^2_{\log P} & 0 \\ 0 & b^2_e \end{bmatrix}, \tag{A6}$$

where $b_{\log P}$ and b_e are the 'rule-of-thumb' (Silverman 1986) bandwidth parameters that determine how much we 'smooth' the distribution. We choose $e_{\rm max} = 1$, $e_{\rm min} = 0$, $\log(P_{\rm min}\,{\rm d}^{-1}) = -6$ and $\log(P_{\rm max}\,{\rm d}^{-1}) = 4$ for our analysis.

The log-likelihoods fluctuate by $\mathcal{O}(1)$ depending on the choice of bandwidth. This systematic uncertainty in the estimated likelihoods arises because our theoretical distributions are built from a finite number of samples, and could be improved with larger simulation campaigns.

[6] We found that density maps estimated via a 2D binned histogram, as used by Andrews et al. (2015), were extremely sensitive to the chosen number of bins.

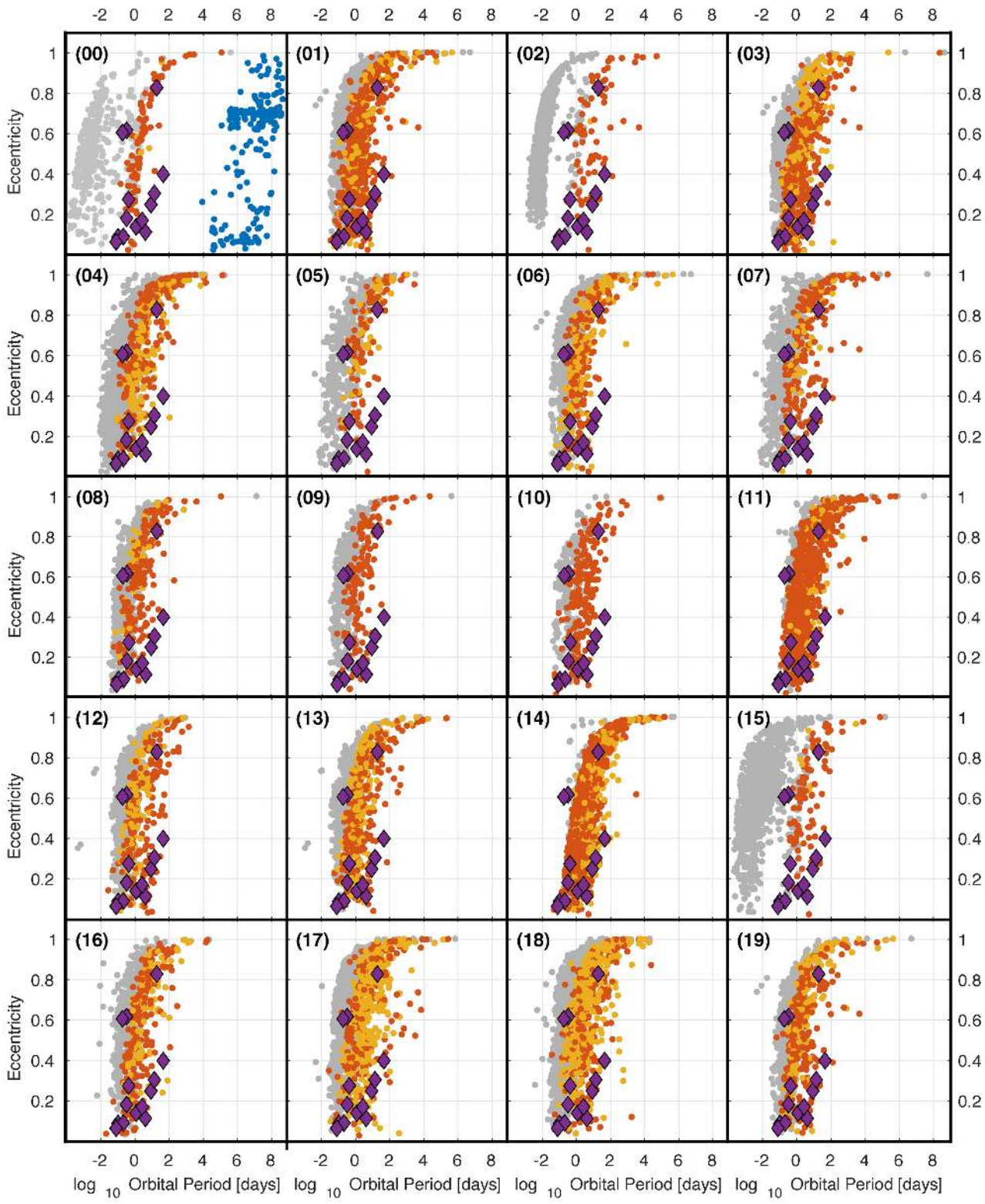

Figure A1. Predicted *P–e* distribution of Galactic DNSs under the `Fiducial` model. Grey dots are all DNS at DCO formation. DCO period and eccentricity are evolved forward from birth until present age given gravitational-wave radiation emission, likely removing short-lived short-period binaries from the observable population. Coloured dots represent the DNS distribution at present age. Colour denotes the type of CE phase: blue for no CE phase, red for a single-core and yellow for a double-core CE phase. The single-core and double-core can be, in most cases, associated with *Channel I* and *Channel* II, respectively (see Section 3.1.1). Purple diamonds represent the observed Galactic DNSs; all observed systems have precise *P–e* measurements with error bars within the thickness of the symbol.

APPENDIX B: MODEL FOR THE DEPENDENCE OF THE KICK VELOCITY ON EXPLOSION PARAMETERS

The most viable mechanism for producing sizeable natal kicks in CCSN explosions is the gravitational tug-boat mechanism, which relies on the acceleration of the NS due to the net gravitational pull exerted by anisotropic ejecta during the first few seconds after shock revival (Scheck et al. 2004, 2006; Nordhaus et al. 2010; Wongwathanarat, Janka & Müller 2013). Bray & Eldridge (2016) suggested that this natal kick could be correlated with other explosion properties. An attempt to clarify these correlations based on the phenomenology of multidimensional simulations was then made by Janka (2017), whose natal kick estimate we briefly review here, since it largely agrees with the one we developed for COMPAS. Invoking total momentum conservation, Janka (2017) considered the momentum $|\boldsymbol{p}_{\rm ej}|$ of the ejecta at a time when the natal kick asymptotes to its final value. Introducing an anisotropy parameter $\alpha_{\rm kick}$ to relate $|\boldsymbol{p}_{\rm ej}|$ to the spherical quasi-momentum of the ejecta as

$$\alpha_{\rm kick} = \frac{|\boldsymbol{p}_{\rm ej}|}{\int_{\rm ejecta} \rho |\boldsymbol{v}| \, {\rm d}V}, \tag{B1}$$

Janka (2017) then invoked dimensional analysis to relate the ejecta (and NS) momentum to the kinetic energy $E_{\rm kin}$ and mass $m_{\rm ej}$ of the anisotropic ejecta behind the shock as

$$|\boldsymbol{p}_{\rm ej}| = \alpha_{\rm kick} \sqrt{2 E_{\rm kin} m_{\rm ej}}. \tag{B2}$$

In the early phase when the natal kick is determined, $E_{\rm kin}$ is of the order of the diagnostic explosion energy $E_{\rm expl}$ (i.e. the net energy of unbound material), within a factor of 2–3 in recent 3D neutrino hydrodynamics simulations. Unlike Janka (2017), we simply identify $E_{\rm kin}$ and $E_{\rm expl}$ so that we obtain the natal kick velocity $v_{\rm kick}$ as

$$v_{\rm kick} = \frac{\alpha_{\rm kick} \sqrt{2 E_{\rm expl} m_{\rm ej}}}{m_{\rm NS}}, \tag{B3}$$

where $m_{\rm NS}$ is the gravitational NS mass. To obtain $m_{\rm ej}$, Janka (2017) related $E_{\rm expl}$ to the mass m_ν of the *neutrino-heated* ejecta via the nucleon recombination energy and then expressed $m_{\rm ej}$ as a multiple thereof. The semi-analytical models of Müller et al. (2016) directly predict $m_{\rm ej}$, $E_{\rm expl}$, and $m_{\rm NS}$ (see below), up to parameters based on 3D simulations and observational constraints. These parameters are calibrated slightly differently than in Müller et al. (2016) (see Section 3.2.4). We can therefore work directly with equation (B3).

Equation (B3) needs to be evaluated at the time when the natal kick asymptotes to its final value. One possibility, suggested by Janka (2017), is to relate the freeze-out of the natal kick to the termination of accretion on to the NS, which happens roughly when the post-shock velocity equals the escape velocity (Marek & Janka 2009; Müller et al. 2016); this is the criterion we adopt here.

Our key assumption is that the expectation value of the anisotropy parameter $\alpha_{\rm kick}$ is independent of the progenitor. This is based on the observation that 3D explosion models (Lentz et al. 2015; Melson et al. 2015b; Müller et al. 2017) with multigroup neutrino transport typically develop unipolar or bipolar explosions, i.e. there is limited variation in explosion geometry. Moreover, there is a convergence to similar turbulent Mach number around (Summa et al. 2016) and after shock revival, which implies a similar density contrast between the underdense neutrino-heated bubbles and the surrounding down flows. This is somewhat dissimilar from parametrized models (Wongwathanarat et al. 2013), which show larger variations in $\alpha_{\rm kick}$ because they can vary the explosion energy independently of the progenitor structure.

While the assumption of uniform $\alpha_{\rm kick}$ is well motivated, some caveats about its limitations are in order. Even though the

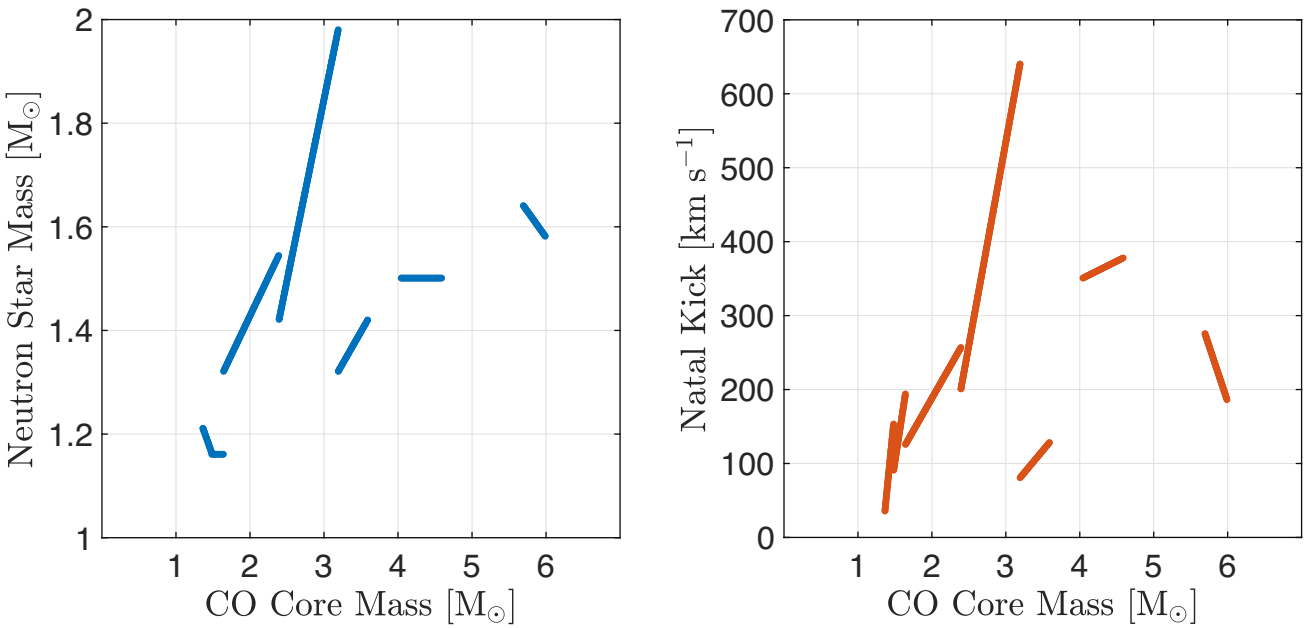

Figure B1. Müller SN prescription of the best-fitting relation to the models described by Müller et al. (2016) with parameters adjusted for better agreement with inferred SN progenitor masses (Smartt 2015). Gravitational mass (left) and natal kick (right) of the NS as a function of the CO core mass. BH formation is assumed to happen for $3.6 \leq m_{\rm CO} < 4.05$, $4.6 \leq m_{\rm CO} < 5.7$, and $m_{\rm CO} > 6.0$, where $m_{\rm CO}$ is the CO core mass in $M_\odot$ units.

distribution of $\alpha_{\rm kick}$ may be relatively uniform across different progenitors (which remains to be confirmed by more 3D explosion models), $\alpha_{\rm kick}$ will show stochastic variations. Moreover, SN models for progenitors with small CO cores are characterized by medium-scale asymmetries (Wanajo, Janka & Müller 2011; Melson, Janka & Marek 2015a) instead of unipolar/bipolar modes during the explosion phase.

Since theoretical arguments can only constrain the assumed uniform value of $\alpha_{\rm kick}$ within an order of magnitude, calibration is still required to roughly match the observed distribution of NS natal kicks. The fit formulae presented below are based on a normalization $\alpha_{\rm kick} = 0.08$ that yields a match to the observed natal kick distribution of Hobbs et al. (2005).

For the NS mass $m_{\rm NS}$, we use

$$\frac{m_{\rm NS}}{\rm M_\odot} = \begin{cases} 1.21 - 0.40(m_{\rm CO} - 1.37), & 1.37 \leq m_{\rm CO} < 1.49 \\ 1.16, & 1.49 \leq m_{\rm CO} < 1.65 \\ 1.32 + 0.30(m_{\rm CO} - 1.65), & 1.65 \leq m_{\rm CO} < 2.40 \\ 1.42 + 0.70(m_{\rm CO} - 2.40), & 2.40 \leq m_{\rm CO} < 3.20 \\ 1.32 + 0.25(m_{\rm CO} - 3.20), & 3.20 \leq m_{\rm CO} < 3.60 \\ 1.50 & 4.05 \leq m_{\rm CO} < 4.60 \\ 1.64 - 0.20(m_{\rm CO} - 5.70), & 5.70 \leq m_{\rm CO} < 6.00 \end{cases}, \quad \text{(B4)}$$

where $m_{\rm CO}$ is the CO core mass in units of $\rm M_\odot$. BH formation is assumed to happen for $3.6 \leq m_{\rm CO} < 4.05$, $4.6 \leq m_{\rm CO} < 5.7$, and $m_{\rm CO} > 6.0$.

The natal kicks are computed as

$$\frac{v_{\rm kick}}{\rm km\,s^{-1}} = \begin{cases} 35 + 1000(m_{\rm CO} - 1.37), & 1.37 \leq m_{\rm CO} < 1.49 \\ 90 + 650(m_{\rm CO} - 1.49), & 1.49 \leq m_{\rm CO} < 1.65 \\ 100 + 175(m_{\rm CO} - 1.65), & 1.65 \leq m_{\rm CO} < 2.40 \\ 200 + 550(m_{\rm CO} - 2.40), & 2.40 \leq m_{\rm CO} < 3.20 \\ 80 + 120(m_{\rm CO} - 3.20), & 3.20 \leq m_{\rm CO} < 3.60 \\ 350 + 50(m_{\rm CO} - 4.05), & 4.05 \leq m_{\rm CO} < 4.60 \\ 275 - 300(m_{\rm CO} - 5.70), & 5.70 \leq m_{\rm CO} < 6.00 \end{cases}. \quad \text{(B5)}$$

APPENDIX C: MOVEMENT IN THE GALACTIC POTENTIAL

DNS centre-of-mass velocities in our `Fiducial` model, in which the second SN is typically a USSN with a low natal kick, are dominated by the Blaauw kick received as a result of the mass-loss accompanying the collapse of the secondary. This kick is proportional to the orbital velocity of the secondary before the collapse, which is greatest for the most compact binaries. Therefore, the binary's velocity is anticorrelated with the coalescence time, as shown on the left-hand panel of Fig. C1. If the USSN progenitors are stripped even deeper than in COMPAS models during case BB mass transfer Tauris et al. (2015), as discussed in Section 4, the mass lost during the SN and the associated Blaauw kick would be further reduced.

These kicks have the effect of broadening the distribution of observed DNS systems in the Galaxy. We assume that each DNS is formed in the thin disc, at $z = 0$ in cylindrical coordinates, with a radial distribution proportional to the disc mass projected on to the Galactic equatorial plane. We use model 2 of Irrgang et al. (2013) for the Galactic matter distribution and total gravitational potential. We do not account for scattering in this simplified analysis; while dynamical heating would increase the scale height of older populations, it does not appreciably impact the distribution of distances from the Galactic centre, which we estimate here. After choosing a random initial location for the binary as above, we apply an additional initial velocity relative to the local rotational velocity with a magnitude equal to the binary's simulated kick velocity and a random direction. The trajectory of the binary in the Galactic potential is solved with a Runge–Kutta integrator. We sample the binary's subsequent motion at fixed time intervals between birth and merger (or a maximum age of 10 Gyr). The right-hand panel of Fig. C1 shows the cumulative distribution function of the birth location, and the broader cumulative distribution function at which DNS systems are expected to reside for a snapshot of all DNSs existing at the present moment. The broadening of the distribution would be more significant in shallower gravitational potentials of less massive galaxies, which are probed with short GRBs.

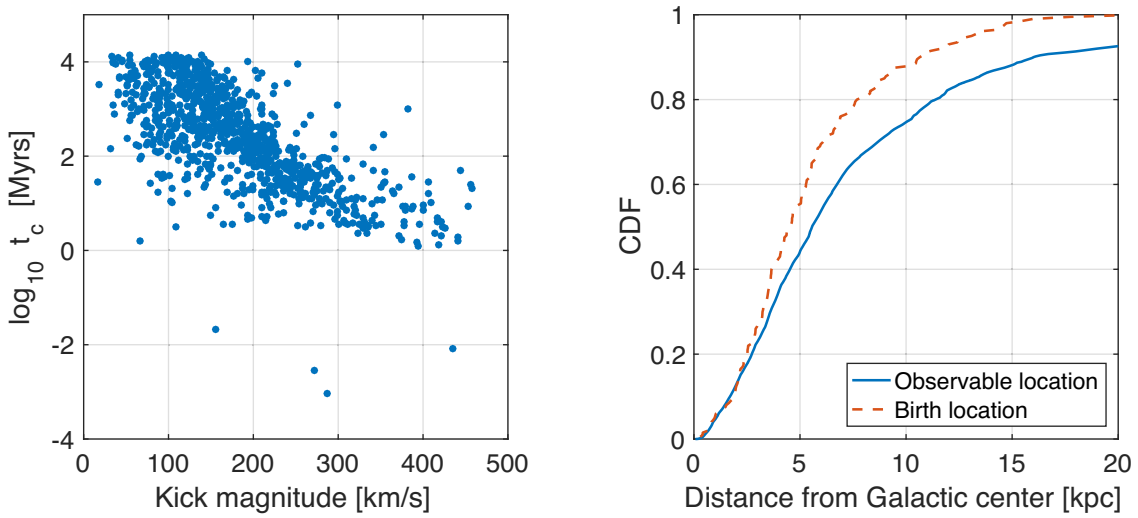

Figure C1. Scatter plot of the binary coalescence time against the DNS kicks magnitude in the `Fiducial` model (left-hand panel). DNS kicks are dominated by the Blaauw kick during the collapse of the secondary, which is proportional to the orbital velocity of the progenitor and therefore inversely correlated with the coalescence time of the binary. These kicks spread the binaries in the Milky Way gravitational potential relative to birth sites, which are presumed to be in the disc plane (cumulative distribution function of the Galacto-centric distance for binaries born in the disc is shown in the right-hand panel).

This paper has been typeset from a TEX/LATEX file prepared by the author.